A Penalization-Regularization-Operator Splitting Method for Eikonal Based Traveltime Tomography[*]

Roland Glowinski[†], Shingyu Leung[‡], and Jianliang Qian[§]

Abstract. We propose a new methodology for carrying out eikonal based traveltime tomography arising from important applications such as seismic imaging and medical imaging. The new method formulates the traveltime tomography problem as a variational problem for a certain cost functional explicitly with respect to both traveltime and sound speed. Furthermore, the cost functional is penalized to enforce the nonlinear equality constraint associated with the underlying eikonal equation, biharmonically regularized with respect to traveltime, and harmonically regularized with respect to sound speed. To overcome the difficulty associated with the inherent nonlinearity of the eikonal equation, the Euler–Lagrange equation of the penalized-regularized variational problem is reformulated into an equivalent, mixed optimality system. This mixed system is associated with an initial value problem which is solved by an operator-splitting based solution method, and the splitting approach effectively reduces the optimality system into three nonlinear subproblems and three linear subproblems. Moreover, the nonlinear subproblems can be solved pointwise, while the linear subproblems can be reduced to linear second-order elliptic problems. Numerical experiments show that the new method can carry out traveltime tomography successfully and recover sound speeds efficiently.

Key words. eikonal equations, traveltime tomography, fast sweeping methods, penalization, regularization, operator splitting

AMS subject classifications. 65Y10, 47G30

DOI. 10.1137/140992072

1. Introduction. Traveltime tomography is a class of important inverse problems arising from a variety of applications, such as seismic imaging, medical imaging, nondestructive testing, and underwater acoustics. Given the traveltime data between sources and receivers, traveltime tomography posed as an inverse problem aims to recover the sound speed of the underlying interior medium between sources and receivers from traveltime measurements. Since there may exist multiple ray paths to connect a source and a receiver, traveltime tomography may be formulated as first-arrival (single-arrival) based or multiarrival based inverse problems, which correspond to boundary rigidity or lens rigidity problems in differential geometry, respectively. In this article, given first-arrival traveltime boundary data, we develop

a penalization-regularization-operator splitting method for eikonal based traveltime tomography.

Traditional traveltime tomography methods mostly rely on ray-tracing to compute traveltimes between sources and receivers so as to fit the traveltime data [23]. Ray-tracing based approaches have at least two shortcomings: first, since the Hamiltonian system for computing ray paths is very sensitive to initial conditions, and it is generally difficult to control where a ray goes, it is a nontrivial task to assign traveltimes from a source to all receivers by ray-tracing in numerical simulations; second, Fermat-principle based shooting methods for two-point boundary value problems between a source and a receiver may fail to converge. Consequently, some alternative methods are sought to avoid explicit ray-tracing. Based on the eikonal solvers for first-arrival traveltimes [42], Ammon and Vidale [1] developed a traveltime tomography method without rays by computing explicitly the discretized Fréchet derivative of first-arrival traveltime with respect to sound speed. To avoid computing Fréchet derivatives directly, Sei and Symes [31, 32] proposed an adjoint-state method for traveltime tomography based on paraxial eikonal equations. Later on, Leung and Qian [14] developed adjoint-state methods systematically for traveltime tomography based on eikonal equations, and this adjoint state method has been further developed in [39, 11, 16, 17]. The success of all these eikonal based first-arrival traveltime tomography methods heavily relies on robust and efficient eikonal solvers, which have been extensively developed in the last two decades [42, 41, 29, 30, 10, 33, 27, 28, 43, 40, 13, 12, 19, 18]. So the question is, can we develop an efficient algorithm for traveltime tomography without eikonal solvers or ray-tracing? In this article, we specifically attempt to develop such a method by proposing new variational formulations for eikonal based traveltime tomography so that an efficient penalization-regularization-operator splitting methodology can be applied to solve the underlying inverse problems.

Suppose that traveltime tomography is posed as a least-squares data fitting problem. Then the inverse problem is to find a suitable sound speed to minimize the mismatch between measured and simulated traveltimes in the least-squares sense. While the adjoint-state method for first-arrival traveltime tomography [14] may be viewed as some kind of primal-dual formulation of least-squares traveltime tomography in the sense that the solution of the adjoint-state equation is a Lagrange multiplier, the penalization-regularization approach proposed here may be viewed as a least-squares primal formulation. So a natural question is, what are the advantages of the new approach over the adjoint-state approach? The adjoint-state method has at least two drawbacks that are frequently overlooked. The first is associated with the theoretical question of well-posedness of the adjoint-state equation, as the equation is in conservation form with possible discontinuous coefficients defined by the gradient of traveltime, which is the viscosity solution of the eikonal equation; there is no known well-posedness result for such an equation. The second is that, because traveltime tomography is a complicated problem, it is unlikely that the discretized adjoint equation is really the adjoint equation of the discrete problem, as derivations of adjoint and discretization do not commute in general. Nevertheless, these two drawbacks of the adjoint-state method [14] do not deter us from using the method, as it has already been successfully applied in practice [39, 11]. On the other hand, the least-squares primal formulation proposed here does not have those shortcomings, as all the equations involved are well understood.

As is well known, given first-arrival traveltime measurements, ray-tracing based traveltime tomography may not be able to simulate first-arrival traveltimes so as to fit the data, while the adjoint-state method [14] indeed simulates first-arrivals to fit the given data. So the question is, does the penalization-regularization approach proposed here simulate first-arrival traveltimes to fit the given data? In [5] and [8] an analogous approach for solving Dirichlet problems for eikonal equations is shown to yield a (kind of) viscosity solution in a Stokes sense (at least in two dimensions). Moreover, our current numerical examples strongly indicate that the new approach also simulates first-arrival traveltimes to fit the given data, so the corresponding solution for the eikonal equation may be a viscosity solution in the sense of Crandall and Lions [4]. We will report theoretical results for this question in a future publication.

Theoretically, viewed as a boundary rigidity problem, first-arrival traveltime tomography consists in determining a compact Riemannian manifold with boundary up to an action of a diffeomorphism which is the identity at the boundary, by knowing the geodesic distance function between boundary points (see [21, 22, 20, 24, 34] and references therein). One needs an a priori hypothesis to determine this since it is easy to find counterexamples if the index of refraction is too large in certain regions. An a priori condition that has been proposed is simplicity of the metric [20]. A manifold is simple if the boundary is strictly convex with respect to the Riemannian metric and there are no conjugate points along any geodesic. So far, it seems to be difficult to handle the case with conjugate points since they are related to the so-called caustics and multiarrivals in geometrical optics [34, 35, 36]. In practice, we do not know in advance whether the Riemannian metric defined by the underlying sound speed is simple or not. Consequently, the available first-arrival traveltime information may not suffice to determine the sound speed so that the resulting sound speed model may have limited resolution when the to-be-imaged structure is very complicated, and this can be observed in our numerical results for the Marmousi model. To improve resolution of traveltime tomography, we have to take into account multiarrivals as demonstrated in [15, 2, 3]. It is an ongoing effort to develop a penalization-regularization approach for multiarrival traveltime tomography.

Our new method formulates the traveltime tomography problem as a variational problem for a certain cost functional explicitly with respect to both traveltime and sound speed. Furthermore, the cost functional is penalized to enforce the nonlinear equality constraint associated with the underlying eikonal equation, biharmonically regularized with respect to traveltime, and harmonically regularized with respect to sound speed. To overcome the difficulty associated with the inherent nonlinearity of the eikonal equation, the Euler–Lagrange equation of the penalized-regularized variational problem is reformulated into an equivalent, mixed optimality system. This mixed system is associated with an initial value problem which is solved by an operator-splitting based solution method, and the splitting approach efficiently reduces the optimality system into three nonlinear subproblems and three linear subproblems. Moreover, the nonlinear subproblems can be solved pointwise, and the linear subproblems can be reduced to linear second-order elliptic problems. Numerical experiments show that the new method can carry out traveltime tomography successfully and recover sound speeds efficiently.

2. Problem formulations. Let Ω be a bounded domain of $\mathbb{R}^d$ ($d = 2$ or 3 in practice); we denote by Γ the boundary of Ω. The problem is to find a function c_{opt} of x such that

$$(2.1) \qquad\qquad c_{\text{opt}} \in \mathcal{C}, \quad J(c_{\text{opt}}) \leq J(c) \quad \forall c \in \mathcal{C},$$

where the convex set $\mathcal{C}$ is defined by

$$\mathcal{C} = \{c : c \in L^2(\Omega), 0 < c_{\min} \leq c(x) \leq c_{\max} \text{ a.e. on } \Omega\};$$

the cost function J is defined by

$$J(c) = \frac{1}{2} \int_\Gamma |z - y_d|^2 d\Gamma,$$

where z is the solution of the *eikonal equation* problem

(2.2)
$$\begin{cases} |\nabla z| = \frac{1}{c} & \text{in } \Omega, \\ z \geq 0, \\ z(x_s) = 0, & x_s \in \Omega. \end{cases}$$

Let us denote c^{-2} by v; then problem (2.1) is clearly equivalent to

(2.3)
$$\begin{cases} \text{find } \{y, u\} \in E \text{ such that} \\ j(y, u) \leq j(z, v) \quad \forall \{z, v\} \in E, \end{cases}$$

where the functional j is defined by

(2.4)
$$j(z, v) = \frac{1}{2} \int_\Gamma |z - y_d|^2 d\Gamma,$$

and the set E is defined by
(2.5)
$$E = \left\{ \{z, v\} : z \in W^{1,\infty}(\Omega), z \geq 0, z(x_s) = 0, |\nabla z|^2 = v, 0 < \frac{1}{c_{\max}^2} \leq v(x) \leq \frac{1}{c_{\min}^2} \text{ a.e. on } \Omega \right\}.$$

Actually, there is equivalence between (2.3) and

(2.6)
$$\begin{cases} \text{find } \{y, u\} \in E \text{ such that} \\ j_C(y, u) \leq j_C(z, v) \quad \forall \{z, v\} \in E, \end{cases}$$

where $C > 0$ and

(2.7)
$$j_C(z, v) = \frac{1}{2} \int_\Omega |\nabla z|^2 dx - \frac{1}{2} \int_\Omega v dx + \frac{C}{2} \int_\Gamma |z - y_d|^2 d\Gamma.$$

From now on we will assume that $y_d \geq 0$, and will denote $c_{\max}^{-2}$ (resp., $c_{\min}^{-2}$) by a (resp., b).

Following [5] and [8], we advocate for the solution of the *constrained minimization problem* (2.6) a methodology combining *penalization, regularization,* and *operator-splitting.* Let us introduce first $\epsilon = \{\epsilon_1, \epsilon_2, \epsilon_3\}$, with ϵ_i's being small positive numbers. We approximate problem (2.6) by a *less constrained* problem, namely,

(2.8)
$$\begin{cases} \text{find } \{y, u\} \in V_0^+ \times K \text{ such that} \\ j_C^\epsilon(y, u) \leq j_C^\epsilon(z, v) \quad \forall \{z, v\} \in V_0^+ \times K, \end{cases}$$

where

(2.9) $\qquad V_0^+ = \{z : \nabla^2 z \in L^2(\Omega), z \in W^{1,4}(\Omega), z(x_s) = 0, z \geq 0\},$

(2.10) $\qquad K = \{v : v \in H^1(\Omega), a \leq v(x) \leq b \text{ a.e. on } \Omega\},$

and

$$j_C^\epsilon(z,v) = \frac{\epsilon_1}{2} \int_\Omega |\nabla^2 z|^2 dx + \frac{1}{2} \int_\Omega |\nabla z|^2 dx + \frac{C}{2} \int_\Gamma |z - y_d|^2 d\Gamma + \frac{\epsilon_2}{2} \int_\Omega |\nabla v|^2 dx$$

(2.11)
$$- \frac{1}{2} \int_\Omega v \, dx + \frac{1}{4\epsilon_3} \int_\Omega ||\nabla z|^2 - v|^2 \, dx.$$

In the above definition of the functional $j_C^\epsilon(z,v)$, the last term associated with ϵ_3 is a penalty term of Ginzburg–Landau type, used to enforce the eikonal equation treated as an equality constraint. The regularization terms associated with ϵ_1 and ϵ_2 are used to control possible oscillations of the solution. If v is taken to be fixed, the functional $j_C^\epsilon(z,v)$ is analogous to a biharmonic regularization technique used in [5] and [8], which leads to viscosity solutions of the eikonal equation in the sense of Stokes (at least in two dimensions).

Using *continuity*, *convexity,* and *compactness* arguments we can easily show that the minimization problem (2.8) has a solution.

We remark that the convex set V_0^+ is the positive cone of the space V_0 defined by

$$V_0 = \{z : \nabla^2 z \in L^2(\Omega), z \in W^{1,4}(\Omega), z(x_s) = 0\}.$$

Since the injection of $W^{1,4}(\Omega)$ in $C^0(\bar\Omega)$ is continuous if $d = 2$ and 3 (indeed, it is compact), V_0 (resp., V_0^+) is a closed subspace (resp., closed convex subset) of the space $W^{1,4}(\Omega) \cap H(\Omega, \nabla^2)$, with $H(\Omega, \nabla^2) = \{z : z \in L^2, \nabla^2 z \in L^2(\Omega)\}$.

In the following section we are going to provide a system of optimality conditions verified by a solution $\{y, u\}$ of (2.8); this is an essential step toward the iterative solution of the above problem.

3. Optimality conditions for problem (2.8). Using classical tools from calculus of variations, we can easily show that any solution $\{y, u\}$ of problem (2.8) has to verify the following coupled system of elliptic variational inequalities:

(3.1) $\begin{cases} y \in V_0^+, \\ \epsilon_1 \int_\Omega \nabla^2 y \nabla^2(z - y) dx + \int_\Omega \nabla y \cdot \nabla(z - y) dx + C \int_\Gamma (y - y_d)(z - y) d\Gamma \\ \quad + \frac{1}{\epsilon_3} \int_\Omega (|\nabla y|^2 - u) \nabla y \cdot \nabla(z - y) dx \geq 0 \quad \forall z \in V_0^+, \end{cases}$

(3.2) $\begin{cases} u \in K, \\ \epsilon_2 \int_\Omega \nabla u \cdot \nabla(v - u) dx + \frac{1}{2\epsilon_3} \int_\Omega (u - |\nabla y|^2)(v - u) dx - \frac{1}{2} \int_\Omega (v - u) dx \geq 0 \quad \forall v \in K. \end{cases}$

The main difficulty with the above system is related to the cubic nonlinear term $|\nabla y|^2 \nabla y$ in (3.1). To overcome this difficulty we are going to introduce the vector-valued function $\mathbf{p} = \nabla y$ and transfer the nonlinearity burden from y to $\mathbf{p}$ via an appropriate equivalent reformulation of system (3.1)–(3.2). Next, we will associate to this new optimality system an initial value

problem to be time-discretized by an operator-splitting scheme decoupling nonlinearities and those differential operators involving the space variables.

Let us introduce the convex set $\mathbf{W}^+$ defined by

$$\mathbf{W}^+ = \left\{ \{z, \mathbf{q}\} : z \in V_0^+, \mathbf{q} \in \left(L^4(\Omega) \right)^d, \mathbf{q} = \nabla z \right\}.$$

There is then equivalence between the optimality system (3.1)–(3.2) and

(3.3) $\begin{cases} \{y, \mathbf{p}\} \in \mathbf{W}^+, \\ \epsilon_1 \int_\Omega \nabla \cdot \mathbf{p} \nabla \cdot (\mathbf{q} - \mathbf{p}) dx + \int_\Omega \mathbf{p} \cdot (\mathbf{q} - \mathbf{p}) dx + C \int_\Gamma (y - y_d)(z - y) d\Gamma \\ \quad + \frac{1}{\epsilon_3} \int_\Omega \left(|\mathbf{p}|^2 - u \right) \mathbf{p} \cdot (\mathbf{q} - \mathbf{p}) dx \geq 0 \quad \forall \{z, \mathbf{q}\} \in \mathbf{W}^+, \end{cases}$

(3.4) $\begin{cases} u \in K, \\ \epsilon_2 \int_\Omega \nabla u \cdot \nabla (v - u) dx + \frac{1}{2\epsilon_3} \int_\Omega (u - |\mathbf{p}|^2)(v - u) dx - \frac{1}{2} \int_\Omega (v - u) dx \geq 0 \quad \forall v \in K. \end{cases}$

Actually, the above system can be reformulated itself as the following, which is better suited to an operator-splitting based solution method:

(3.5) $\begin{cases} \{y, \mathbf{p}\} \in V_0^+ \times \left(L^4(\Omega) \right)^d, \\ \epsilon_1 \int_\Omega \nabla \cdot \mathbf{p} \nabla \cdot (\mathbf{q} - \mathbf{p}) dx + \int_\Omega \mathbf{p} \cdot (\mathbf{q} - \mathbf{p}) dx + C \int_\Gamma (y - y_d)(z - y) d\Gamma \\ \quad + \frac{1}{\epsilon_3} \int_\Omega (|\mathbf{p}|^2 - u) \mathbf{p} \cdot (\mathbf{q} - \mathbf{p}) dx + \langle \partial I_\nabla(y, \mathbf{p}), \{z - y, \mathbf{q} - \mathbf{p}\} \rangle \geq 0 \\ \forall \{z, \mathbf{q}\} \in V_0^+ \times \left(L^4(\Omega) \right)^d, \end{cases}$

(3.6) $\begin{cases} u \in H^1(\Omega), \\ \epsilon_2 \int_\Omega \nabla u \cdot \nabla v dx + \frac{1}{2\epsilon_3} \int_\Omega (u - |\mathbf{p}|^2) v dx - \frac{1}{2} \int_\Omega v dx + \langle \partial I_{\tilde{K}}(u), v \rangle = 0 \\ \forall v \in H^1(\Omega), \end{cases}$

where, in (3.5)–(3.6), ∂I_∇ (resp., $\partial I_{\tilde{K}}$) denotes the subgradient of the indicator functional I_∇ (resp., $I_{\tilde{K}}$) with

(3.7) $$I_\nabla(z, \mathbf{q}) = \begin{cases} 0 \text{ if } \{z, \mathbf{q}\} \in \mathbf{W}^+, \\ +\infty \text{ otherwise} \end{cases}$$

(resp.,

(3.8) $$I_{\tilde{K}}(v) = \begin{cases} 0 \text{ if } v \in \tilde{K}, \\ +\infty \text{ otherwise} \end{cases}$$

with $\tilde{K} = \{v : v \in L^2(\Omega), a \leq v(x) \leq b, \text{ a.e. in } \Omega\}$.

In order to capture the steady state solution by solving (3.5)–(3.6), we associate with this system the following initial value problem (*flow* in the dynamical system terminology): For $\{\{y_0, \mathbf{p}_0\}, u_0\} \in \mathbf{W}^+ \times K$, find $\forall t \in (0, +\infty)$, $\{y(t), \mathbf{p}(t), u(t)\} \in V_0^+ \times \left(L^4(\Omega) \right)^d \times H^1(\Omega)$,

verifying

$$(3.9) \quad \begin{cases} \{y(0), \mathbf{p}(0)\} = \{y_0, \mathbf{p}_0\}(\in \mathbf{W}^+), \\ \int_\Omega \frac{\partial \mathbf{p}(t)}{\partial t} \cdot (\mathbf{q} - \mathbf{p}(t)) dx + \epsilon_1 \int_\Omega \nabla \cdot \mathbf{p}(t) \nabla \cdot (\mathbf{q} - \mathbf{p}(t)) dx + \int_\Omega \mathbf{p}(t) \cdot (\mathbf{q} - \mathbf{p}(t)) dx \\ \quad + C \int_\Gamma (y(t) - y_d)(z - y(t)) d\Gamma + \frac{1}{\epsilon_3} \int_\Omega (|\mathbf{p}(t)|^2 - u(t)) \mathbf{p}(t) \cdot (\mathbf{q} - \mathbf{p}(t)) dx \\ \quad + \langle \partial I_\nabla(y(t), \mathbf{p}(t)), \{z - y(t), \mathbf{q} - \mathbf{p}(t)\} \rangle \geq 0 \quad \forall \{z, \mathbf{q}\} \in V_0^+ \times \left(L^4(\Omega)\right)^d; \end{cases}$$

$$(3.10) \quad \begin{cases} u(0) = u_0(\in K), \\ \frac{1}{\gamma} \int_\Omega \frac{\partial u(t)}{\partial t} v dx + \epsilon_2 \int_\Omega \nabla u(t) \cdot \nabla v dx + \frac{1}{2\epsilon_3} \int_\Omega (u(t) - |\mathbf{p}(t)|^2) v dx - \frac{1}{2} \int_\Omega v dx \\ \quad + \langle \partial I_{\tilde{K}}(u(t)), v \rangle = 0 \quad \forall v \in H^1(\Omega). \end{cases}$$

In the above, we have used the notation $\varphi(t)$ for the function $x \to \varphi(x, t)$, and $\gamma \ (> 0)$ is a scaling factor. In order to adjust γ, we need to remember that, ideally,

$$(3.11) \qquad\qquad\qquad\qquad |\mathbf{p}|^2 = u.$$

Differentiating with respect to t, we obtain from (3.11) that $2\mathbf{p} \cdot \frac{\partial \mathbf{p}}{\partial t} = \frac{\partial u}{\partial t}$, which implies in turn that (with $[\cdot]$ denoting dimension)

$$(3.12) \qquad\qquad \left[\frac{\partial \mathbf{p}}{\partial t}\right] = \left[\frac{1}{|\mathbf{p}|} \frac{\partial u}{\partial t}\right] = \left[\frac{1}{\sqrt{u}} \frac{\partial u}{\partial t}\right].$$

Relation (3.12) suggests taking for γ the square root of one of the three natural means of a and b, that is,

$$\gamma_1 = \sqrt{\frac{a+b}{2}}, \quad \gamma_2 = \sqrt[4]{ab}, \quad \text{and } \gamma_3 = \sqrt{\frac{2ab}{a+b}}.$$

Other mean values make sense, with the simplest one being $\gamma_4 = (\sqrt{a} + \sqrt{b})/2$. Actually, before any testing to justify this choice, we like γ_2.

In order to solve the initial value problem (3.9)–(3.10) for t varying from 0 to $+\infty$, we are going to employ a symmetrized operator-splitting scheme reminiscent of the one introduced by Strang in [37] (see also [6] and [9]). This will be discussed in the following section.

4. An operator-splitting scheme for the time discretization of problem (3.9)–(3.10).
For the time discretization of the initial value problem (3.9)–(3.10), we suggest the following symmetrized operator-splitting scheme, where $\Delta t \ (> 0)$ is a time discretization step and where $t^{n+\alpha}$ denotes $(n + \alpha)\Delta t$; the other notation is classical. Taking into account (3.7) and (3.8), we may time-discretize (3.9)–(3.10) as follows (other schemes are possible as shown in Remark 4.1):

$$(4.1) \qquad\qquad \{y^0, \mathbf{p}^0\} = \{y_0, \mathbf{p}_0\}, \quad u^0 = u_0$$

(thus we have $\mathbf{p}^0 = \nabla y^0$).

For $n \geq 0$, the time marching from $\{y^n, \mathbf{p}^n, u^n\} \to \{y^{n+1}, \mathbf{p}^{n+1}, u^{n+1}\}$ can be carried out as follows. We first solve the following elliptic variational inequalities:

(4.2)
$$\begin{cases} y^{n+1/2} \in V_0^+ \,, \\ \int_\Omega \frac{\nabla y^{n+1/2} - \mathbf{p}^n}{\Delta t/2} \cdot \nabla(z - y^{n+1/2})dx + \epsilon_1 \int_\Omega \nabla^2 y^{n+1/2} \nabla^2(z - y^{n+1/2})dx \\ \quad + \int_\Omega \nabla y^{n+1/2} \cdot \nabla(z - y^{n+1/2})dx + C \int_\Gamma (y^{n+1/2} - y_d)(z - y^{n+1/2})d\Gamma \geq 0 \quad \forall z \in V_0^+ \,, \end{cases}$$

and, with $\mathbf{p}^{n+1/2} = \nabla y^{n+1/2}$,

(4.3)
$$\begin{cases} u^{n+1/2} \in \tilde{K} \,, \\ \frac{1}{\gamma} \int_\Omega \frac{u^{n+1/2} - u^n}{\Delta t/2}(v - u^{n+1/2})dx + \frac{1}{2\epsilon_3} \int_\Omega (u^{n+1/2} - |\mathbf{p}^{n+1/2}|^2)(v - u^{n+1/2})dx \\ \quad - \frac{1}{2} \int_\Omega (v - u^{n+1/2})dx \geq 0 \quad \forall v \in \tilde{K} \,, \end{cases}$$

then

(4.4)
$$\begin{cases} \hat{\mathbf{p}}^{n+1/2} \in \left(L^4(\Omega)\right)^d \,, \\ \int_\Omega \frac{\hat{\mathbf{p}}^{n+1/2} - \mathbf{p}^{n+1/2}}{\Delta t} \cdot \mathbf{q}dx + \frac{1}{\epsilon_3} \int_\Omega (|\hat{\mathbf{p}}^{n+1/2}|^2 - u^{n+1/2})\hat{\mathbf{p}}^{n+1/2} \cdot \mathbf{q}dx = 0 \quad \forall \mathbf{q} \in \left(L^4(\Omega)\right)^d \,, \end{cases}$$

(4.5)
$$\begin{cases} \hat{u}^{n+1/2} \in H^1(\Omega) \,, \\ \frac{1}{\gamma} \int_\Omega \frac{\hat{u}^{n+1/2} - u^{n+1/2}}{\Delta t}vdx + \epsilon_2 \int_\Omega \nabla \hat{u}^{n+1/2} \cdot \nabla vdx = 0 \quad \forall v \in H^1(\Omega) \,, \end{cases}$$

and finally,

(4.6)
$$\begin{cases} y^{n+1} \in V_0^+ \,, \\ \int_\Omega \frac{\nabla y^{n+1} - \hat{\mathbf{p}}^{n+1/2}}{\Delta t/2} \cdot \nabla(z - y^{n+1})dx + \epsilon_1 \int_\Omega \nabla^2 y^{n+1} \nabla^2(z - y^{n+1})dx \\ \quad + \int_\Omega \nabla y^{n+1} \cdot \nabla(z - y^{n+1})dx + C \int_\Gamma (y^{n+1} - y_d)(z - y^{n+1})d\Gamma \geq 0 \quad \forall z \in V_0^+ \,, \end{cases}$$

and, with $\mathbf{p}^{n+1} = \nabla y^{n+1}$,

(4.7)
$$\begin{cases} u^{n+1} \in \tilde{K} \,, \\ \frac{1}{\gamma} \int_\Omega \frac{u^{n+1} - \hat{u}^{n+1/2}}{\Delta t/2}(v - u^{n+1})dx + \frac{1}{2\epsilon_3} \int_\Omega (u^{n+1} - |\mathbf{p}^{n+1}|^2)(v - u^{n+1})dx \\ \quad - \frac{1}{2} \int_\Omega (v - u^{n+1})dx \geq 0 \quad \forall v \in \tilde{K} \,. \end{cases}$$

Remark 4.1. A variant of scheme (4.1)–(4.7) is obtained by replacing (4.4)–(4.5) by

(4.8)
$$\begin{cases} \hat{u}^{n+1/2} \in H^1(\Omega) \,, \\ \frac{1}{\gamma} \int_\Omega \frac{\hat{u}^{n+1/2} - u^n}{\Delta t}vdx + \epsilon_2 \int_\Omega \nabla \hat{u}^{n+1/2} \cdot \nabla vdx = 0 \quad \forall v \in H^1(\Omega) \,, \end{cases}$$

(4.9)
$$\begin{cases} \hat{\mathbf{p}}^{n+1/2} \in \left(L^4(\Omega)\right)^d \,, \\ \int_\Omega \frac{\hat{\mathbf{p}}^{n+1/2} - \mathbf{p}^{n+1/2}}{\Delta t} \cdot \mathbf{q}dx + \frac{1}{\epsilon_3} \int_\Omega (|\hat{\mathbf{p}}^{n+1/2}|^2 - \hat{u}^{n+1/2})\hat{\mathbf{p}}^{n+1/2} \cdot \mathbf{q}dx = 0 \quad \forall \mathbf{q} \in \left(L^4(\Omega)\right)^d \,. \end{cases}$$

Remark 4.2. Another variant of scheme (4.1)–(4.7) is obtained by imposing the condition $y(x_s, t) = 0$ only once per time step. In that case we suggest keeping it in (4.2) (for regularity

reasons). In that case, one has to replace V_0^+ in (4.6) by the convex set $\{z : \nabla^2 z \in L^2(\Omega), z \in W^{1,4}(\Omega), z \geq 0\}$.

We are going to discuss the solution of the subproblems encountered at the fractional steps of scheme (4.1)–(4.7) (the solution methods to be discussed still apply if one replaces (4.4)–(4.5) by (4.8)–(4.9)).

Remark 4.3. Preliminary numerical experiments have shown that if $y_d \geq 0$ and if the discrete analogue of the initial value problem (3.9)–(3.10) is properly initialized, there is no need to impose the condition $y \geq 0$ in (3.1)–(3.2) to obtain nonnegative functions y^n from algorithm (4.1)–(4.7). We will take advantage of this observation in section 4.4 when discussing the solution of problems (4.3) and (4.6).

4.1. Solving the nonlinear subproblems (4.3) and (4.7). Dropping the superscripts shows that both problems (4.3) and (4.7) are particular cases of

(4.10)
$$\begin{cases} u \in \tilde{K}, \\ \int_\Omega (u - w)(v - u)dx + \gamma \frac{\Delta t}{4\epsilon_3} \int_\Omega (u - |\mathbf{p}|^2)(v - u)dx - \gamma \frac{\Delta t}{4} \int_\Omega (v - u)dx \geq 0 \quad \forall v \in \tilde{K}. \end{cases}$$

It follows from [7] that (4.10) characterizes u as the unique solution of the following constrained minimization problem:

(4.11)
$$\begin{cases} \text{find } u \in \tilde{K} \text{ such that} \\ j_1(u) \leq j_1(v) \quad \forall v \in \tilde{K}, \end{cases}$$

where

(4.12)
$$j_1(v) = \frac{1}{2}\left(1 + \gamma\frac{\Delta t}{4\epsilon_3}\right)\int_\Omega |v|^2 dx - \int_\Omega \left(w + \gamma\frac{\Delta t}{4\epsilon_3}|\mathbf{p}|^2 + \gamma\frac{\Delta t}{4}\right)v\,dx,$$

with the functions w and $\mathbf{p}$ given.

The functional j_1 can be minimized pointwise over Ω; doing so, we obtain

(4.13)
$$u(x) = \inf\left[b, \sup\left(a, \frac{w(x) + \gamma\frac{\Delta t}{4\epsilon_3}|\mathbf{p}(x)|^2 + \gamma\frac{\Delta t}{4}}{1 + \gamma\frac{\Delta t}{4\epsilon_3}}\right)\right] \quad \text{a.e. on } \Omega.$$

4.2. Solving the nonlinear subproblem (4.4). Problem (4.4) is a particular case of

(4.14)
$$\begin{cases} \mathbf{p} \in \left(L^4(\Omega)\right)^d, \\ \int_\Omega \left(1 - \frac{\Delta t}{\epsilon_3}u\right)\mathbf{p}\cdot\mathbf{q}\,dx + \frac{\Delta t}{\epsilon_3}\int_\Omega |\mathbf{p}|^2\,\mathbf{p}\cdot\mathbf{q}\,dx = \int_\Omega \mathbf{r}\cdot\mathbf{q}\,dx \quad \forall \mathbf{q} \in \left(L^4(\Omega)\right)^d, \end{cases}$$

where u and $\mathbf{r}$ are two given functions with $a \leq u \leq b$ as defined above. Suppose that

(4.15)
$$\Delta t \leq \frac{\epsilon_3}{b};$$

then the nonlinear variational problem (4.14) has a unique solution (actually, we can easily show that if $\mathbf{r}$ belongs to $\left(L^4(\Omega)\right)^d$, which is clearly the case if $\mathbf{r} = \mathbf{p}^{n+1/2}$, then $\mathbf{p}$ belongs to $\left(L^6(\Omega)\right)^d$).

Formulation (4.14) implies that

$$(4.16) \qquad \left(1 - \frac{\Delta t}{\epsilon_3} u(x)\right) \mathbf{p}(x) + \frac{\Delta t}{\epsilon_3} |\mathbf{p}(x)|^2 \mathbf{p}(x) = \mathbf{r}(x) \quad \text{a.e. in } \Omega.$$

Problem (4.16) can be solved pointwise. Indeed, since $1 - \frac{\Delta t}{\epsilon_3} u(x) \geq 0$ a.e. in Ω (from (4.15)), we observe that $|\mathbf{p}(x)|$ is the unique solution (necessarily nonnegative) of the cubic equation

$$(4.17) \qquad \left(1 - \frac{\Delta t}{\epsilon_3} u(x)\right) z + \frac{\Delta t}{\epsilon_3} z^3 = |\mathbf{r}(x)|.$$

Once $|\mathbf{p}(x)|$ is known, it follows from (4.16) that

$$(4.18) \qquad \mathbf{p}(x) = \frac{\mathbf{r}(x)}{\left(1 - \frac{\Delta t}{\epsilon_3} u(x)\right) + \frac{\Delta t}{\epsilon_3} |\mathbf{p}(x)|^2} \quad \text{a.e. in } \Omega.$$

To solve the cubic equation (4.17), we advocate using Newton's method initialized by $\sqrt[3]{\frac{\epsilon_3}{\Delta t} |\mathbf{r}(x)|}$.

4.3. Solving the linear subproblem (4.5). Problem (4.5) is a particular case of

$$\begin{cases} u \in H^1(\Omega), \\ \int_\Omega uv dx + \Delta t\epsilon_2 \int_\Omega \nabla u \cdot \nabla v dx = \int_\Omega wv dx \quad \forall v \in H^1(\Omega), \end{cases}$$

where w is a given function. Actually, this problem is nothing but the variational formulation of the following very classical Neumann problem:

$$(4.19) \qquad \begin{cases} u - \Delta t\epsilon_2 \nabla^2 u = w \text{ in } \Omega, \\ \frac{\partial u}{\partial n} = 0 \text{ on } \Gamma. \end{cases}$$

4.4. Solving the subproblems (4.2) and (4.6). Since we decided not to take into account the positivity of y (see Remark 4.3 for a justification), the variational inequalities (4.2) and (4.6) reduce (formally) to linear variational problems of the type

$$(4.20) \qquad \begin{cases} y \in Z_0, \\ \left(1 + \frac{\Delta t}{2}\right) \int_\Omega \nabla y \cdot \nabla z dx + \frac{\Delta t}{2}\epsilon_1 \int_\Omega \nabla^2 y \nabla^2 z dx + \frac{\Delta t}{2} C \int_\Gamma yz d\Gamma \\ = \int_\Omega \mathbf{p} \cdot \nabla z dx + \frac{\Delta t}{2} C \int_\Gamma gz d\Gamma \quad \forall z \in Z_0, \end{cases}$$

where $\mathbf{p}$ and g are given functions and $Z_0 = \{z : z \in H^2(\Omega), z(x_s) = 0\}$. Actually, associating a Lagrange multiplier with the relation $y(x_s) = 0$, we see that there is equivalence between (4.20) and the variational system

$$(4.21) \qquad \begin{cases} \{y, \lambda\} \in H^2(\Omega) \times \mathbb{R}, \\ \left(1 + \frac{\Delta t}{2}\right) \int_\Omega \nabla y \cdot \nabla z dx + \frac{\Delta t}{2}\epsilon_1 \int_\Omega \nabla^2 y \nabla^2 z dx + \frac{\Delta t}{2} C \int_\Gamma yz d\Gamma \\ = \int_\Omega \mathbf{p} \cdot \nabla z dx + \frac{\Delta t}{2} C \int_\Gamma gz d\Gamma + \lambda z(x_s) \quad \forall z \in H^2(\Omega), \\ y(x_s) = 0. \end{cases}$$

The above formulation makes sense since, if $d = 1$, 2, and 3, the injection of $H^2(\Omega)$ into $C^0(\bar{\Omega})$ is compact.

In order to solve (4.20), we are going to identify the elliptic equation verified by the unique solution of (4.20) and the associated boundary conditions. The usual approach is to take, in (4.21), z in the space $\mathcal{D}(\Omega)$ ($\subset H^2(\Omega)$) of the C^∞ functions with compact support in Ω. We then have, since $z = 0$ on Γ,

$$(4.22) \quad \left(1 + \frac{\Delta t}{2}\right) \int_\Omega \nabla y \cdot \nabla z \, dx + \frac{\Delta t}{2} \epsilon_1 \int_\Omega \nabla^2 y \nabla^2 z \, dx = \int_\Omega \mathbf{p} \cdot \nabla z \, dx + \lambda z(x_s) \quad \forall z \in \mathcal{D}(\Omega).$$

It follows from (4.22) that y is the solution, in the sense of distributions, of

$$(4.23) \quad -\left(1 + \frac{\Delta t}{2}\right) \nabla^2 y + \frac{\Delta t}{2} \epsilon_1 \nabla^4 y = -\nabla \cdot \mathbf{p} + \lambda \delta_{(x_s)},$$

where $\delta_{(x_s)}$ is the Dirac measure at x_s. In order to recover the boundary conditions associated with the biharmonic equation (4.23), we multiply both sides of (4.23) by z in $H^2(\Omega)$ and apply (formally) Green's formulas; we obtain first

$$(4.24) \quad -\left(1 + \frac{\Delta t}{2}\right) \int_\Omega \nabla^2 y z \, dx + \frac{\Delta t}{2} \epsilon_1 \int_\Omega \nabla^4 y z \, dx = -\int_\Omega \nabla \cdot \mathbf{p} z \, dx + \lambda z(x_s),$$

and then, from (4.24),

$$
\begin{aligned}
& \left(1 + \frac{\Delta t}{2}\right) \int_\Omega \nabla y \cdot \nabla z \, dx - \left(1 + \frac{\Delta t}{2}\right) \int_\Gamma \frac{\partial y}{\partial \mathbf{n}} z \, d\Gamma \\
& + \frac{\Delta t}{2} \epsilon_1 \int_\Omega \nabla^2 y \nabla^2 z \, dx + \frac{\Delta t}{2} \epsilon_1 \int_\Gamma \frac{\partial \nabla^2 y}{\partial \mathbf{n}} z \, d\Gamma - \frac{\Delta t}{2} \epsilon_1 \int_\Gamma \nabla^2 y \frac{\partial z}{\partial \mathbf{n}} d\Gamma \\
(4.25) \quad & = \int_\Omega \mathbf{p} \cdot \nabla z \, dx - \int_\Gamma \mathbf{p} \cdot \mathbf{n} z \, d\Gamma + \lambda z(x_s) \quad \forall z \in H^2(\Omega).
\end{aligned}
$$

Comparing relations (4.21) and (4.25) yields

$$
\begin{aligned}
& \left(1 + \frac{\Delta t}{2}\right) \int_\Gamma \frac{\partial y}{\partial \mathbf{n}} z \, d\Gamma - \frac{\Delta t}{2} \epsilon_1 \int_\Gamma \frac{\partial \nabla^2 y}{\partial \mathbf{n}} z \, d\Gamma \\
(4.26) \quad & + \frac{\Delta t}{2} \epsilon_1 \int_\Gamma \nabla^2 y \frac{\partial z}{\partial \mathbf{n}} d\Gamma - \int_\Gamma \mathbf{p} \cdot \mathbf{n} z \, d\Gamma = \frac{\Delta t}{2} C \int_\Gamma (g - y) z \, d\Gamma \quad \forall z \in H^2(\Omega),
\end{aligned}
$$

where, in (4.26), $\mathbf{n}$ is the outward to Ω unit normal vector at Γ. Since $z|_\Gamma$ and $\frac{\partial z}{\partial \mathbf{n}}\big|_\Gamma$ can be arbitrary in the boundary spaces $H^{3/2}(\Gamma)$ and $H^{1/2}(\Gamma)$, respectively, it follows from (4.26) that the solution y of problem (4.21) verifies the following system of boundary conditions:

$$(4.27) \quad \begin{cases} \left(1 + \frac{\Delta t}{2}\right) \frac{\partial y}{\partial \mathbf{n}} - \frac{\Delta t}{2} \epsilon_1 \frac{\partial \nabla^2 y}{\partial \mathbf{n}} + C \frac{\Delta t}{2} y = C \frac{\Delta t}{2} g + \mathbf{p} \cdot \mathbf{n} \text{ on } \Gamma, \\ \nabla^2 y = 0 \text{ on } \Gamma. \end{cases}$$

Collecting the above results shows that the pair $\{y, \lambda\}$ solution of the variational system (4.21) is also the solution of the following biharmonic boundary value problem:

(4.28)
$$\begin{cases} -\left(1 + \frac{\Delta t}{2}\right)\nabla^2 y + \frac{\Delta t}{2}\epsilon_1\nabla^4 y = -\nabla \cdot \mathbf{p} + \lambda\delta_{(x_s)} \text{ in } \Omega, \\ \left(1 + \frac{\Delta t}{2}\right)\frac{\partial y}{\partial \mathbf{n}} - \frac{\Delta t}{2}\epsilon_1\frac{\partial\nabla^2 y}{\partial \mathbf{n}} + C\frac{\Delta t}{2}y = C\frac{\Delta t}{2}g + \mathbf{p} \cdot \mathbf{n} \text{ on } \Gamma, \\ \nabla^2 y = 0 \text{ on } \Gamma, \\ y(x_s) = 0. \end{cases}$$

Solving problem (4.28) is the only nontrivial part of our methodology; the boundary conditions in particular appear frightening. Actually, the biharmonic problem (4.28) is (relatively) easy to solve, the trick being to introduce the function $\omega = -\nabla^2 y$. Then, problem (4.28) is equivalent to the following system:

(4.29)
$$\begin{cases} \left(1 + \frac{\Delta t}{2}\right)\omega - \frac{\Delta t}{2}\epsilon_1\nabla^2\omega = -\nabla \cdot \mathbf{p} + \lambda\delta_{(x_s)} \text{ in } \Omega, \\ \omega = 0 \text{ on } \Gamma, \end{cases}$$

(4.30)
$$\begin{cases} -\nabla^2 y = \omega \text{ in } \Omega, \\ \left(1 + \frac{\Delta t}{2}\right)\frac{\partial y}{\partial \mathbf{n}} + C\frac{\Delta t}{2}y = C\frac{\Delta t}{2}g + \mathbf{p} \cdot \mathbf{n} - \frac{\Delta t}{2}\epsilon_1\frac{\partial\omega}{\partial \mathbf{n}} \text{ on } \Gamma, \\ y(x_s) = 0. \end{cases}$$

The boundary condition verified by y in (4.30) is of Robin type. The two elliptic problems in (4.29)–(4.30) are classical ones; they are well-suited for finite element based solution methods. Of course, an important issue is the adjustment of λ in (4.29)–(4.30); this issue will be discussed in section 4.5, below.

Remark 4.4. An equivalent variational formulation of problem (4.30) reads as follows:

(4.31)
$$\begin{cases} y \in H^2(\Omega), \\ \left(1 + \frac{\Delta t}{2}\right)\int_\Omega \nabla y \cdot \nabla z dx + C\frac{\Delta t}{2}\int_\Gamma yz d\Gamma = C\frac{\Delta t}{2}\int_\Gamma gz d\Gamma + \int_\Omega \mathbf{p} \cdot \nabla z dx \\ \quad -\epsilon_1\frac{\Delta t}{2}\int_\Omega \nabla\omega \cdot \nabla z dx + \lambda z(x_s) \quad \forall z \in H^2(\Omega), \\ y(x_s) = 0. \end{cases}$$

Once ω is known, computing y via (4.31) is rather simple.

Remark 4.5. The computed y in (4.30) is the approximate traveltime solving the eikonal equation equipped with the currently reconstructed velocity at the current point source x_s, and this traveltime is not the same as the viscosity solution obtained by solving the eikonal equation directly using the currently available velocity.

4.5. Adjusting λ in (4.29) and (4.30). The solution y of (4.29)–(4.30) is an affine function of λ. Indeed, we have

(4.32)
$$y = Y_0 + \lambda\bar{y}_1,$$

with Y_0 and $\bar{y}_1$ the solutions of

(4.33)
$$\begin{cases} \left(1 + \frac{\Delta t}{2}\right) \omega_0 - \frac{\Delta t}{2} \epsilon_1 \nabla^2 \omega_0 = -\nabla \cdot \mathbf{p} \text{ in } \Omega, \\ \omega_0 = 0 \text{ on } \Gamma, \end{cases}$$

(4.34)
$$\begin{cases} -\nabla^2 Y_0 = \omega_0 \text{ in } \Omega, \\ \left(1 + \frac{\Delta t}{2}\right) \frac{\partial Y_0}{\partial \mathbf{n}} + C \frac{\Delta t}{2} Y_0 = C \frac{\Delta t}{2} g + \mathbf{p} \cdot \mathbf{n} - \frac{\Delta t}{2} \epsilon_1 \frac{\partial \omega_0}{\partial \mathbf{n}} \text{ on } \Gamma, \end{cases}$$

(4.35)
$$\begin{cases} \left(1 + \frac{\Delta t}{2}\right) \bar{\omega}_1 - \frac{\Delta t}{2} \epsilon_1 \nabla^2 \bar{\omega}_1 = \delta_{(x_s)} \text{ in } \Omega, \\ \bar{\omega}_1 = 0 \text{ on } \Gamma, \end{cases}$$

(4.36)
$$\begin{cases} -\nabla^2 \bar{y}_1 = \bar{\omega}_1 \text{ in } \Omega, \\ \left(1 + \frac{\Delta t}{2}\right) \frac{\partial \bar{y}_1}{\partial \mathbf{n}} + C \frac{\Delta t}{2} \bar{y}_1 = -\frac{\Delta t}{2} \epsilon_1 \frac{\partial \bar{\omega}_1}{\partial \mathbf{n}} \text{ on } \Gamma. \end{cases}$$

From (4.32), the value of λ is given by

(4.37)
$$\lambda = -\frac{Y_0(x_s)}{\bar{y}_1(x_s)}.$$

Remark 4.6. If we keep Δt independent of n, we just need to compute ω_0 and Y_0 (twice) at each time step of the operator-splitting scheme (4.1)–(4.7). The functions $\bar{\omega}_1$ and $\bar{y}_1$, being independent of $\mathbf{p}$, and therefore of n, can be computed once and for all. Actually, we just need to store $\bar{y}_1$.

A most important issue that we still have to address is the initialization of the operator-splitting scheme (4.1)–(4.7). This will be done in section 4.6.

4.6. On the initialization of the operator-splitting scheme (4.1)–(4.7). Since we want to simplify our lives by not imposing explicitly the condition $y \geq 0$, picking a proper initialization in (4.1) is a most important issue. Using dimensionality arguments, we suggest defining y_0 as the solution of the biharmonic problem

(4.38)
$$\begin{cases} dD\nabla^4 y_0 - \nabla^2 y_0 = f + \lambda_0 \delta_{(x_s)} & \text{in } \Omega, \\ y_0 = g \text{ on } \Gamma, \quad \nabla^2 y_0 = 0 \text{ on } \Gamma, \quad y_0(x_s) = 0, \end{cases}$$

and taking

(4.39)
$$\mathbf{p}_0 = \nabla y_0.$$

In (4.38), we have the following:
- D is the diameter of Ω, while d is a small-scale characteristic length. Anticipating the space discretization discussion, we suggest taking for d the space discretization step h.
- The function f is a constant function given by

(4.40)
$$f = \sqrt{\frac{1}{2}(a+b)\Lambda_1},$$

where Λ_1 is the smallest eigenvalue of $-\nabla^2$ operating on $H_0^1(\Omega)$. If Ω is the rectangle $(0, L_1) \times (0, L_2)$, we have $\Lambda_1 = \pi^2 \left(L_1^{-2} + L_2^{-2}\right) = (\pi D/|\Omega|)^2$, with $|\Omega| = $ measure of Ω.

Concerning u_0, one can take

$$(4.41) \qquad u_0 = \frac{1}{2}(a + b),$$

but other choices (based on other mean values) are possible.

To solve (4.38), we suggest the following approach, inspired from section 4.5.

(i) Solve

$$(4.42) \qquad \begin{cases} \omega_0 - dD\nabla^2\omega_0 = f \text{ in } \Omega, \\ \omega_0 = 0 \text{ on } \Gamma, \end{cases}$$

$$(4.43) \qquad \begin{cases} -\nabla^2 Y_0 = \omega_0 \text{ in } \Omega, \\ Y_0 = g \text{ on } \Gamma, \end{cases}$$

$$(4.44) \qquad \begin{cases} \omega_1 - dD\nabla^2\omega_1 = \delta_{(x_s)} \text{ in } \Omega, \\ \omega_1 = 0 \text{ on } \Gamma, \end{cases}$$

$$(4.45) \qquad \begin{cases} -\nabla^2 Y_1 = \omega_1 \text{ in } \Omega, \\ Y_1 = g \text{ on } \Gamma. \end{cases}$$

(ii) Compute

$$\lambda_0 = -\frac{Y_0(x_s)}{Y_1(x_s)}.$$

(iii) Finally, set

$$(4.46) \qquad y_0 = Y_0 + \lambda_0 Y_1.$$

Remark 4.7. There are some brute force methods to impose the positivity of the solution, but we would prefer not to use them since they would affect the regularity of the solutions (but we know they are available if needed).

5. Multiple sources and partial measurements. In this section, we consider practical situations: multiple sources and partial measurements.

5.1. Multiple sources. Assuming that a set of point sources located at $x_s^{(i)}$ gives rise to corresponding traveltime measurement $y_d^{(i)}$ on Γ, where $i = 1, 2, \ldots, N$, following the discussion in section 2 the inverse problem is to find a function c_{opt} of x so as to minimize the cost function

$$J(c) = \frac{1}{2N}\sum_{i=1}^{N}\int_{\Gamma}|z^{(i)} - y_d^{(i)}|^2 d\Gamma \quad \forall c \in \mathcal{C},$$

where $z^{(i)}$ is the solution to the eikonal equation satisfying $z(x_s^{(i)}) = 0$. Accordingly, we modify the functional j_C^ϵ to take into account the information of multiple sources,

$$
\begin{aligned}
j_C^\epsilon(z^{(1)}, \ldots, z^{(N)}, v) \\
= \frac{\epsilon_1}{2N} \sum_{i=1}^{N} \int_\Omega |\nabla^2 z^{(i)}|^2 dx + \frac{1}{2N} \sum_{i=1}^{N} \int_\Omega |\nabla z^{(i)}|^2 dx + \frac{C}{2N} \sum_{i=1}^{N} \int_\Gamma |z^{(i)} - y_d^{(i)}|^2 d\Gamma
\end{aligned}
$$

(5.1)
$$
+ \frac{\epsilon_2}{2} \int_\Omega |\nabla v|^2 dx - \frac{1}{2} \int_\Omega v dx + \frac{1}{4N\epsilon_3} \sum_{i=1}^{N} \int_\Omega \left| |\nabla z^{(i)}|^2 - v \right|^2 dx .
$$

This functional can be minimized by solving a modified optimality system analogous to problems (3.9) and (3.10). Since each point source is independent of other sources, we can simply solve the initial value problem (3.9) N times by replacing $y(t)$ by $y^{(i)}(t)$, $\mathbf{p}(t)$ by $\mathbf{p}^{(i)}(t)$, and the measurements y_d by $y_d^{(i)}$ associated to each $x_s^{(i)}$. Meanwhile, we modify problem (3.10) to be

(5.2)
$$
\begin{cases}
\text{letting } u(0) = u_0 (\in K) \\
\quad \text{find } u(t) \in H^1(\Omega) \quad \text{for} \quad t \in (0, \infty) \text{ such that} \\
\quad \frac{1}{\gamma} \int_\Omega \frac{\partial u(t)}{\partial t} v dx + \epsilon_2 \int_\Omega \nabla u(t) \cdot \nabla v dx + \frac{1}{2N\epsilon_3} \sum_{i=1}^{N} \int_\Omega (u(t) - |\mathbf{p}^{(i)}(t)|^2) v dx \\
\quad - \frac{1}{2} \int_\Omega v dx + \langle \partial I_{\tilde{K}}(u(t)), v \rangle = 0 \quad \forall v \in H^1(\Omega) .
\end{cases}
$$

Therefore, the nonlinear subproblems (4.3) and (4.7) reduce to

(5.3)
$$
\begin{cases}
u \in \tilde{K} , \\
\int_\Omega (u - w)(v - u) dx + \gamma \frac{\Delta t}{4N\epsilon_3} \sum_{i=1}^{N} \int_\Omega (u - |\mathbf{p}^{(i)}|^2)(v - u) dx \\
\quad - \gamma \frac{\Delta t}{4} \int_\Omega (v - u) dx \geq 0 \quad \forall v \in \tilde{K} ,
\end{cases}
$$

which leads to

(5.4)
$$
u(x) = \inf \left[b, \sup \left(a, \frac{w(x) + \gamma \frac{\Delta t}{4N\epsilon_3} \sum_{i=1}^{N} |\mathbf{p}^{(i)}(x)|^2 + \gamma \frac{\Delta t}{4}}{1 + \gamma \frac{\Delta t}{4\epsilon_3}} \right) \right] \quad \text{a.e. on } \Omega .
$$

The rest of the tomography algorithm will stay the same. The computational complexity for each time marching iteration from $\{y^n, \mathbf{p}^n, u^n\}$ to $\{y^{n+1}, \mathbf{p}^{n+1}, u^{n+1}\}$ will be approximately linearly proportional to the number of point sources N.

5.2. Partial measurements. When measurements are only available on a subset $\Gamma' \subset \Gamma$, where Γ denotes the whole boundary of Ω, we propose modifying the matching term $\frac{C}{2} \int_\Gamma |z - y_d|^2 d\Gamma$ to be

$$
\frac{1}{2} \int_\Gamma C \cdot 1_{\Gamma'} \cdot |z - y_d|^2 d\Gamma ,
$$

where $1_{\Gamma'}$ defined on the whole set Γ is the characteristic function of the set Γ'. In the numerical implementation, we need only to slightly modify the code by replacing the constant C in (4.30) by $C \cdot 1_{\Gamma'}$, which is a function defined on Γ. The whole algorithm follows.

6. Numerical experiments. The purpose of numerical experiments is to assess effectiveness of the new algorithm on the boundary rigidity problem, namely, the first-arrival based traveltime tomography problem. As we know from [21, 20, 22, 24, 34], the 2-D boundary rigidity problem has a unique solution up to diffeomorphism if the underlying metric is simple. Therefore, we will show two examples to demonstrate that the algorithm can reconstruct the underlying velocity if indeed the underlying metric (velocity) is simple. However, when the underlying metric is not simple, the situation is much more complicated, and the first-arrival traveltime may not carry information for certain interior regions so that the reconstructed velocity model has very limited resolution, and this is demonstrated in two examples with nonsimple metrics.

To fully appreciate the algorithm, we will first assume an ideal situation, where receivers are located on the whole boundary of the computational domain; namely, we will consider the full-aperture case. Numerically, we will assume that the receivers are located at mesh points on the boundary of the domain so that we can use the fast sweeping method to time those receivers, and these traveltime data on the boundary are further used in the new tomography algorithm as the input data. Furthermore, to deal with practical situations, we will also demonstrate several cases where measurements are given only on a part of the whole boundary of the computational domain.

The overall algorithm is implemented based on finite-difference methods, and the free parameters in the algorithm are chosen to be $\epsilon_1 = 0.01$, $\epsilon_2 = 0.1$, $\epsilon_3 = 0.01$, and $C = 1000$.

6.1. A constant velocity model. In this example, the velocity model is constant, $c(x, y) \equiv 1$, which yields a simple metric. The computational domain is $\Omega = (-1, 1)^2$. We consider three sets of sources. In the case of only one source, the point source is located at $(x_s, y_s) = (0, -0.5)$. In the case of five point sources, they are located at $(x_s, y_s) = (0, -0.5)$, $(x_s, y_s) = (\pm 0.4, -0.5)$, and $(\pm 0.8, -0.5)$. In the case of 10 point sources, they are located at $(x_s, y_s) = (0, \pm 0.5), (\pm 0.4, \pm 0.5)$, and $(\pm 0.8, \pm 0.5)$.

Numerically, we implement the algorithm on different discretized meshes: $\Delta x = \Delta y = 1/16$, $1/32$, $1/64$, and $1/128$, respectively. According to the given discretized mesh, we solve the eikonal equation by the fast sweeping method with a mesh 10 times finer so that the receivers at boundary mesh points are assigned first-arrival traveltimes.

Figures 1 and 2 show the results on a mesh of size $\Delta x = \Delta y = 1/128$. Figure 1 shows the sliced comparisons between the exact velocity model and the reconstructed (inverted) velocity model corresponding to different sets of sources. As we can see, the reconstructed velocity model converges to the exact solution as the number of sources increases. Figure 2 shows the sliced comparison between the "exact" traveltime (corresponding to solving the eikonal equation with the exact velocity at the point source $(0, -0.5)$) and the approximate ("inverted") traveltime (corresponding to the currently reconstructed velocity model associated to the source $(0, -0.5)$). As can be observed from the figure, the approximate traveltime as a by-product of the new tomography algorithm matches the exact traveltime very well, implying that the traveltime data are fit very well; in turn, this also implies that the underlying velocity model is well recovered since the constant isotropic metric is simple.

In Figures 3 and 4, we assume that the measurements are given only along $y = 1$. Since the available information is reduced, we expect the reconstructed solutions to be less accurate.
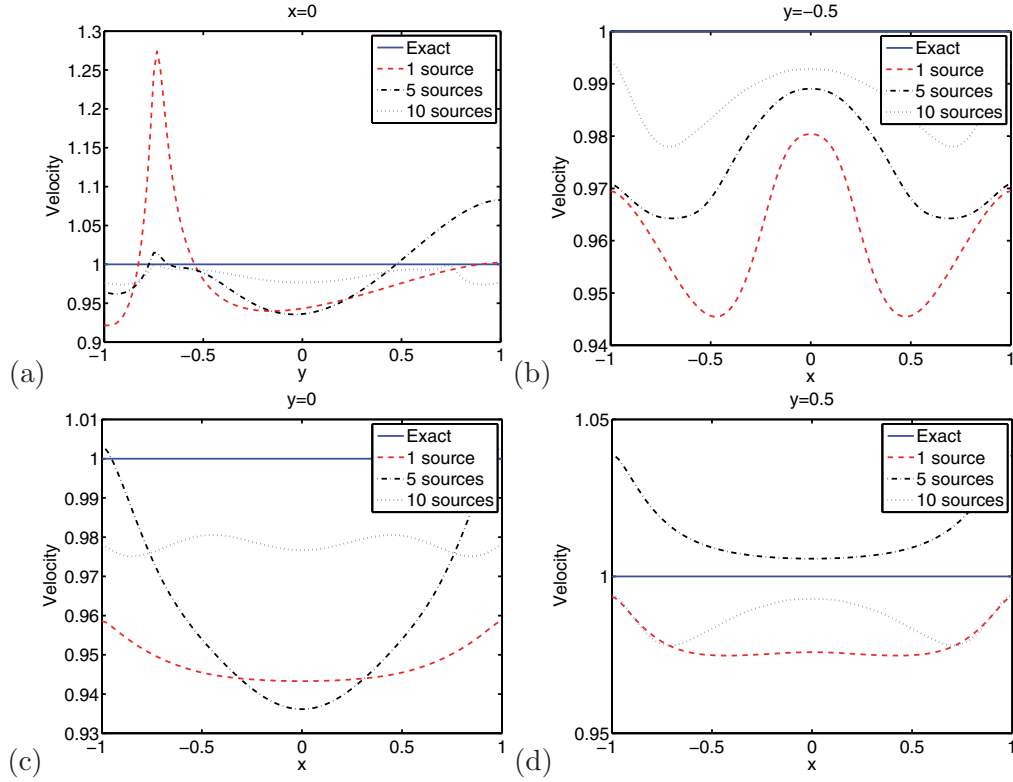
Figure 1. *(Constant velocity model.) Cross sections of the reconstructed velocity along* (a) $x = 0$, (b) $y = -0.5$, (c) $y = 0$, *and* (d) $y = 0.5$.

However, as we increase the number of point sources or refine the underlying mesh, the inverted solutions do match better with the exact solution.

To appreciate the convergence behavior of the new tomography algorithm in terms of mesh sizes, we check the L^2-error of the velocity model and the averaged L^2-error of the traveltime functions, and these two errors are defined as

$$E_{vel}(\Delta x) = \left(\int_\Omega |c_{\mathrm{exact}} - c_{\mathrm{computed}}|^2 \, dx \right)^{1/2} \;,$$

(6.1)
$$E_{tra}(\Delta x) = \frac{1}{N} \left(\sum_{i=1}^N \int_\Omega \left| T^i_{\mathrm{exact}} - T^i_{\mathrm{computed}} \right|^2 dx \right)^{1/2} \;,$$

where c_{exact} is the exact velocity model, c_{computed} is the reconstructed velocity model, T^i_{exact} is the exact traveltime at the source i, T^i_{computed} is the approximate traveltime from the tomography algorithm at the source i, and N is the total number of sources.

Both Figures 5(a) and 5(b) indicate that while keeping the number of sources fixed, increasing the number of receivers (data points located at mesh points on the boundary) allows us to decrease the L^2-fitting errors. At the same time, these figures also show that increasing the number of sources also allows us to decrease L^2-fitting errors while keeping the number of
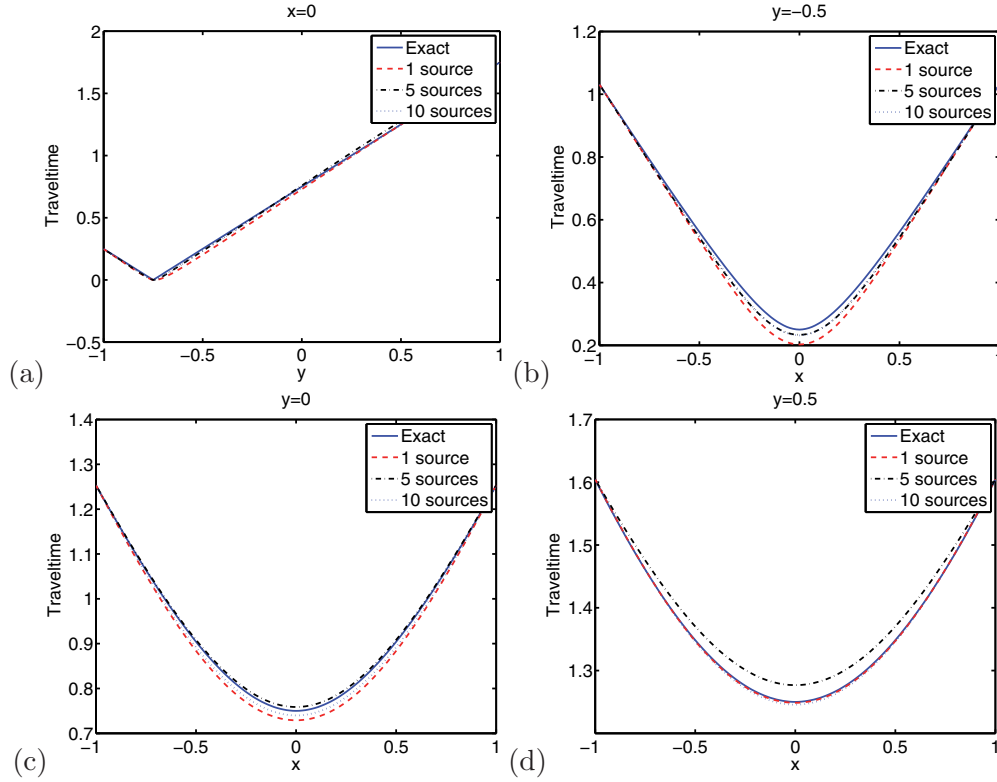
Figure 2. *(Constant velocity model.) Cross sections of the exact traveltime and the approximate traveltime from the point source located at $(0, -0.5)$ along* (a) $x = 0$, (b) $y = -0.5$, (c) $y = 0$, *and* (d) $y = 0.5$.

receivers fixed. Figures 5(c) and 5(d) show the error in the solution when measurements are given only on $y = 1$.

6.2. A linear velocity model. In this example, we consider a linear velocity model: $c(x, y) = 2 + y$. The computational domain is $\Omega = (-1, 1)^2$. We consider three sets of sources. In the case of only one source, the point source is located at $(x_s, y_s) = (0, -0.5)$. In the case of five point sources, they are located at $(x_s, y_s) = (0, -0.5)$, $(x_s, y_s) = (\pm 0.4, -0.5)$, and $(\pm 0.8, -0.5)$. In the case of 10 point sources, they are located at $(x_s, y_s) = (0, \pm 0.5), (\pm 0.4, \pm 0.5)$, and $(\pm 0.8, \pm 0.5)$.

Numerically, we implement the algorithm on a mesh of 41-by-41. Measurements are obtained by solving the eikonal equation using the fast sweeping method on a mesh of 401-by-401. The results are shown in Figures 6 and 7.

Figure 6 shows the sliced comparisons between the exact velocity model and the reconstructed (inverted) velocity model corresponding to different sets of sources. As we can see, the reconstructed velocity model converges to the exact solution as the number of sources increases. Figure 7 shows the sliced comparison between the "exact" traveltime (corresponding to solving the eikonal equation with the exact velocity at the point source $(0, -0.5)$) and the approximate ("inverted") traveltime (corresponding to the currently reconstructed velocity model associated to the source $(0, -0.5)$). As can be observed from the figure, the
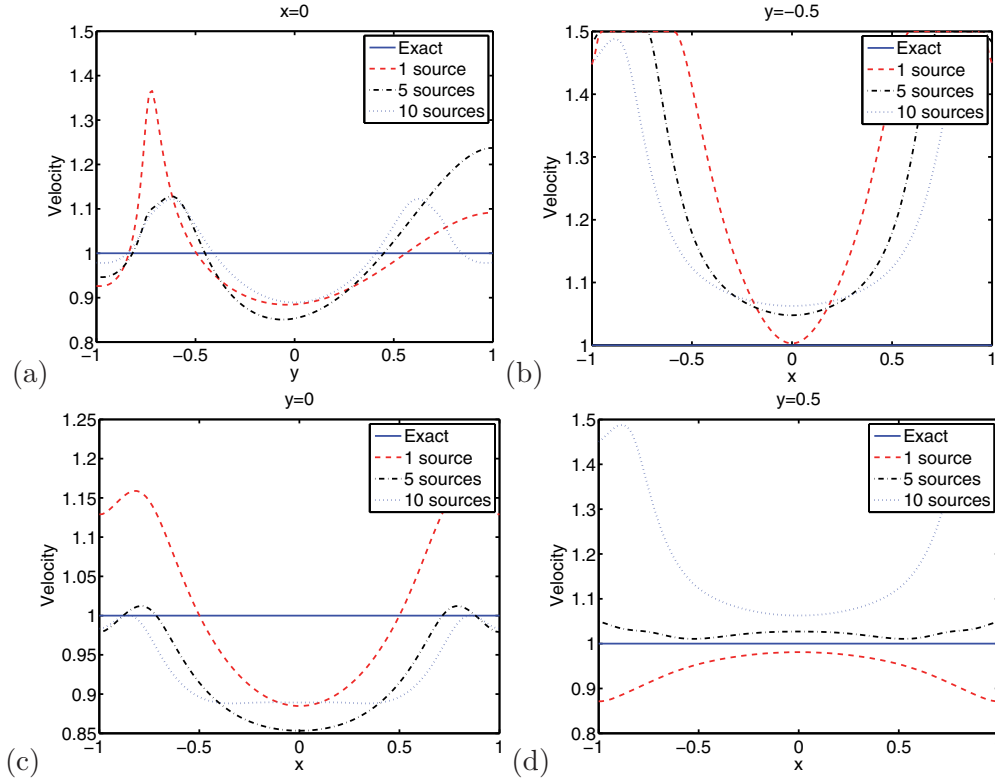
Figure 3. *(Constant model.) Cross sections of the reconstructed velocity along* (a) $x = 0$, (b) $y = -0.5$, (c) $y = 0$, *and* (d) $y = 0.5$ *using measurements along* $y = 1$ *only.*

approximate traveltime as a by-product of the new tomography algorithm matches the exact traveltime very well, implying that the traveltime data are fit very well; in turn, this also implies that the underlying velocity model is well recovered since the underlying metric in the bounded domain is simple.

To appreciate the convergence behavior of the new tomography algorithm in terms of mesh size, we check the L^2-error of the velocity model and the averaged L^2-error of the traveltime functions as defined in (6.1). The different discretized meshes are defined by $\Delta x = \Delta y = 1/16$, $1/32$, $1/64$, and $1/128$, respectively, and the results are shown in Figure 8. The images in Figures 8(a),(b) indicate that, while keeping the number of sources fixed, increasing the number of receivers (data points located at mesh points on the boundary) allows us to decrease the L^2-fitting errors. At the same time, Figures 8(a),(b) also show that increasing the number of sources also allows us to decrease L^2-fitting errors, while keeping the number of receivers fixed.

6.3. A sinusoidal velocity model. This example is adapted from the sinusoidal waveguide model proposed in [38, 25], and the velocity function is given by

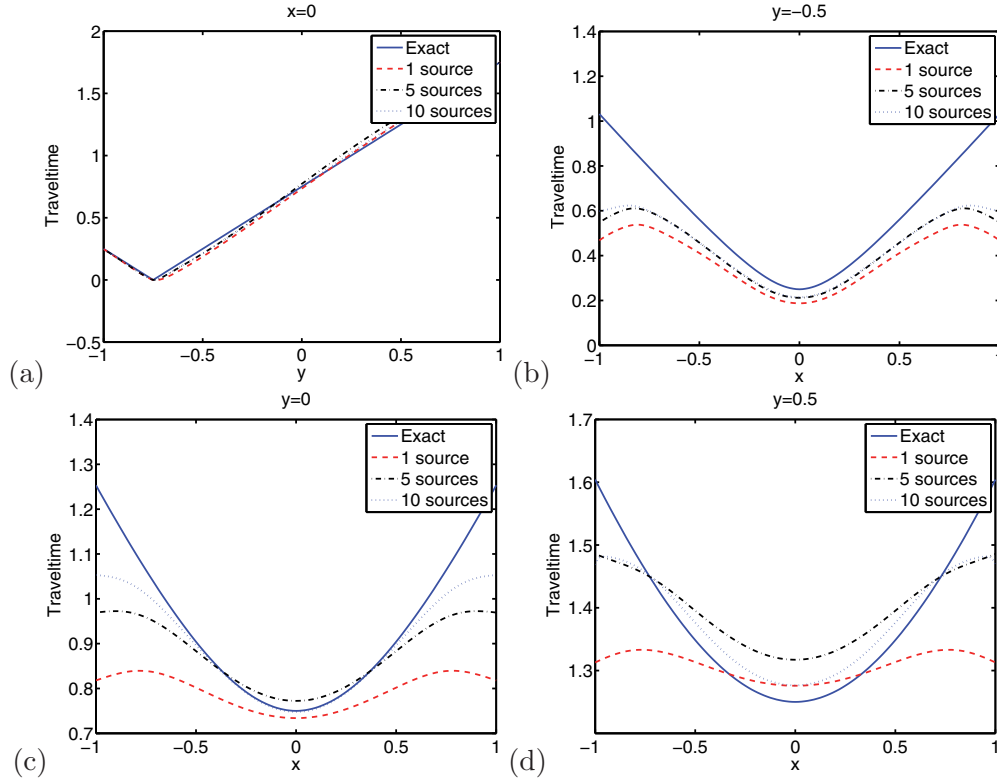$$c(x, y) = 1 + 0.2 \sin[0.5\pi(y + 1)] \sin[3\pi(x + 0.55)].$$

Figure 4. *(Constant velocity model.) Cross sections of the exact traveltime and the approximate traveltime from the point source located at* $(0, -0.5)$ *along* (a) $x = 0$, (b) $y = -0.5$, (c) $y = 0$, *and* (d) $y = 0.5$ *using measurements along* $y = 1$ *only.*

As illustrated in [38, 25], this model shows multiple arrivals and caustics for many source-receiver setups so that the underlying metric is not simple. Therefore, this example serves to illustrate the performance of the new tomography algorithm to recover nonsimple metrics by using only first-arrivals.

The computational domain is $\Omega = (-1, 1])^2$. We consider four sets of sources. In the case of only one source, the point source is located at $(x_s, y_s) = (0, -0.75)$. In the case of five point sources, they are located at $(x_s, y_s) = (0, -0.75)$, $(x_s, y_s) = (\pm 0.4, -0.75)$, and $(\pm 0.8, -0.75)$. In the case of 10 point sources, they are located at $(x_s, y_s) = (0, \pm 0.75), (\pm 0.4, \pm 0.75)$, and $(\pm 0.8, \pm 0.75)$. Finally, when we consider the case with 18 sources, we further add eight more sources at $(x_s, y_s) = (\pm 0.2, \pm 0.75)$ and $(\pm 0.6, \pm 0.75)$ to the case of 10 sources.

Numerically, we implement the algorithm on different discretized meshes $\Delta x = \Delta y = 1/16$, $1/32$, $1/64$, and $1/128$, respectively. According to the given discretized mesh, we solve the eikonal equation by the fast sweeping method with a mesh 10 times finer so that the receivers at boundary mesh points are assigned first-arrival traveltimes.

Figure 9 shows the results on the mesh of $\Delta x = \Delta y = 1/128$ for the case of the single point source at $(x_s, y_s) = (0, -0.75)$. In this case, the velocity model is not reconstructed well, though the approximate traveltime is reasonably analogous to the "exact" first-arrival traveltime at the point source at $(x_s, y_s) = (0, -0.75)$.

Figure 10 shows the results on the mesh of $\Delta x = \Delta y = 1/128$ for the case of 18 sources.
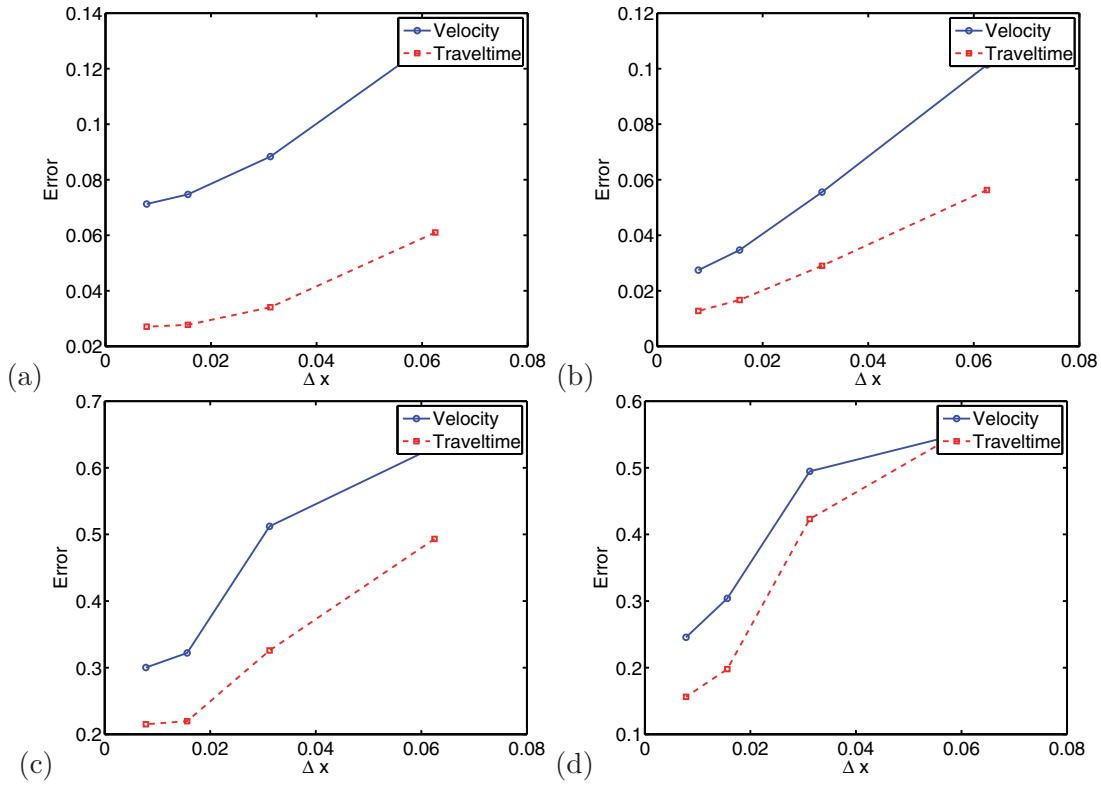
Figure 5. *(Constant velocity model.) Error in the reconstructed velocity and the approximate traveltime fields using* (a) *five and* (b) 10 *point sources with complete measurements. Error in the reconstructed velocity and the approximate traveltime fields using* (c) *five and* (d) 10 *point sources with measurements along* $y = 1$ *only.*

As we can see, the multiple sources based tomography yields a velocity model with much high resolution in comparison to the one-source based tomography. However, because the underlying velocity model is not simple, the first-arrival based tomography yields limited resolution. In terms of traveltimes, we compare that obtained by the direct eikonal solver with that obtained by the tomography algorithm at the point source $(x_s, y_s) = (0, -0.75)$, and the two traveltimes are qualitatively similar.

To further check whether the solution will be improved by refining the mesh in general, we compute the L^2-error (6.1) for the sinusoidal model in Figure 11. Similar to the linear model, the error decreases as we incorporate more measurements into the inverse problem by increasing the number of mesh points.

To appreciate the convergence behavior of the new tomography algorithm in terms of mesh sizes, we check the L^2-error of the velocity model and the averaged L^2-error of the traveltime functions as defined in (6.1). The different discretized meshes are defined by $\Delta x = \Delta y = 1/16$, $1/32$, $1/64$, and $1/128$, respectively, and the results are shown in Figure 11, which indicates that while keeping the number of sources fixed, increasing the number of receivers (data points located at mesh points on the boundary) allows us to decrease the L^2-fitting errors. At the same time, the two figures also show that increasing the number of sources allows us to decrease L^2-fitting errors while keeping the number of receivers fixed.
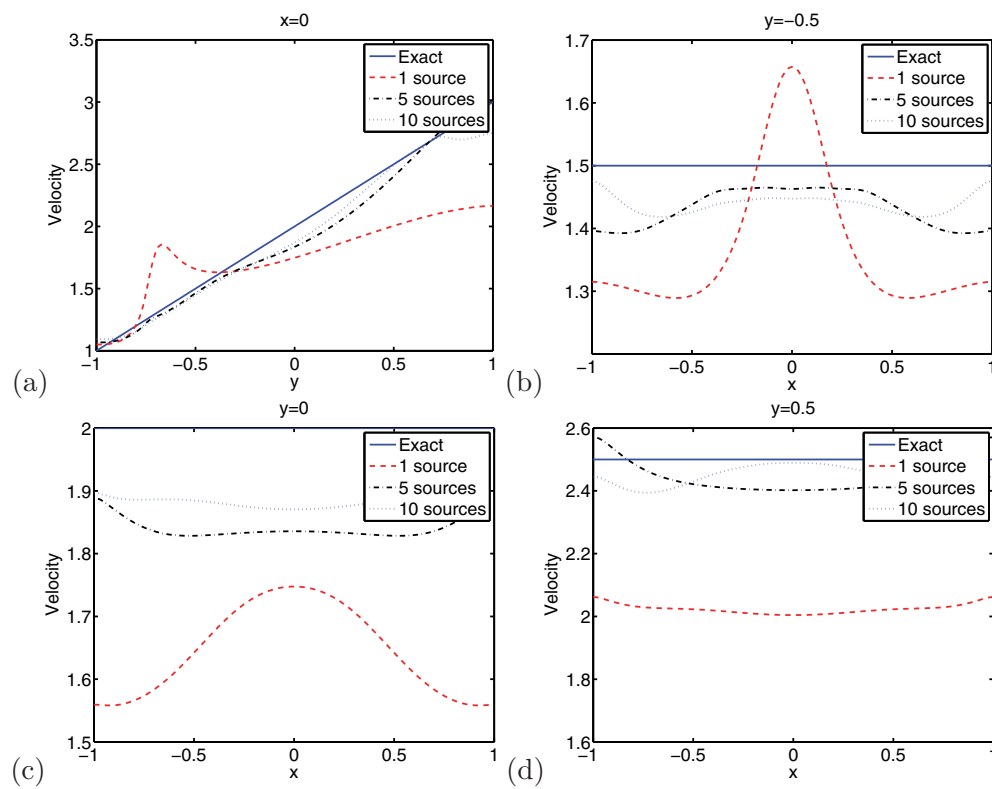
(a) (b) (c) (d)

Figure 6. *(Linear velocity model.) Cross sections of the reconstructed velocity along* (a) $x = 0$, (b) $y = -0.5$, (c) $y = 0$, *and* (d) $y = 0.5$.
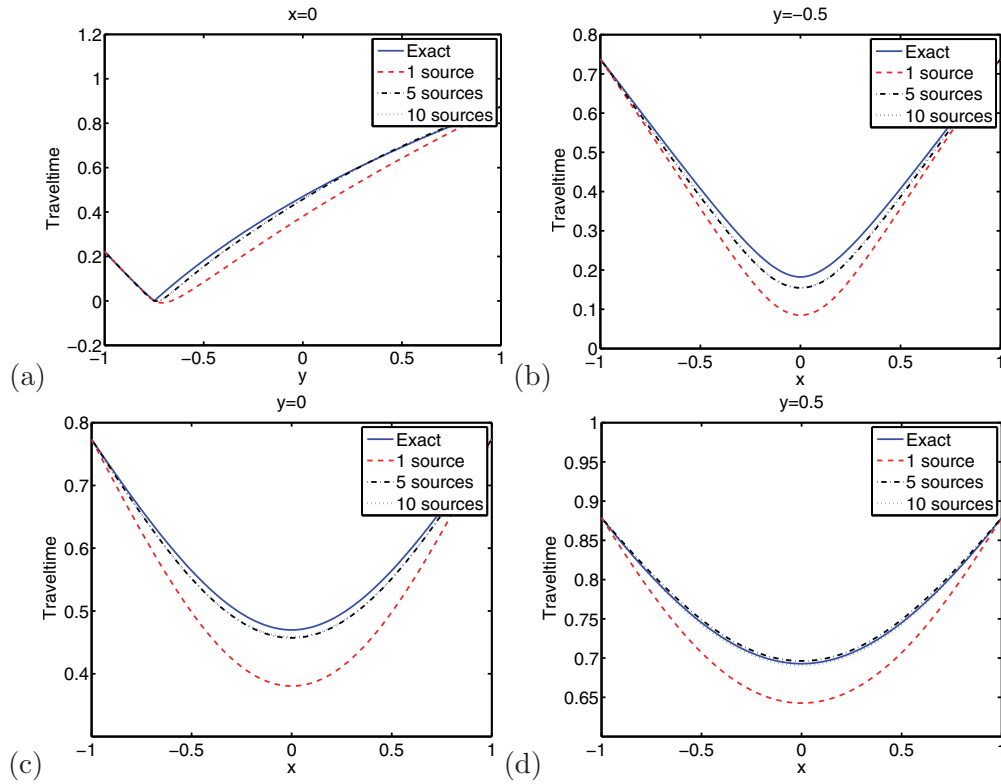
Figure 7. *(Linear velocity model.) Cross sections of the exact traveltime and the approximate traveltime from the point source located at* $(0, -0.5)$ *along* (a) $x = 0$, (b) $y = -0.5$, (c) $y = 0$, *and* (d) $y = 0.5$.
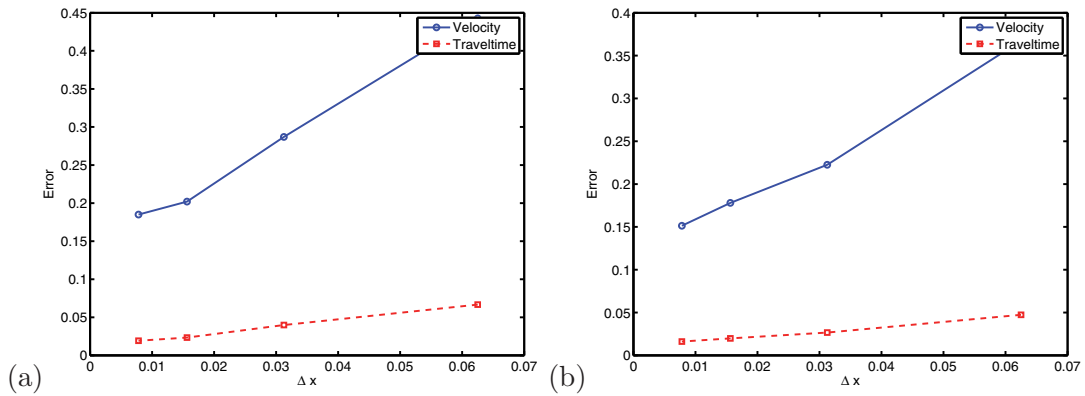

Figure 8. *(Linear velocity model.) Errors in the reconstructed velocity and the approximate traveltime fields using* (a) *five and* (b) 10 *point sources.*
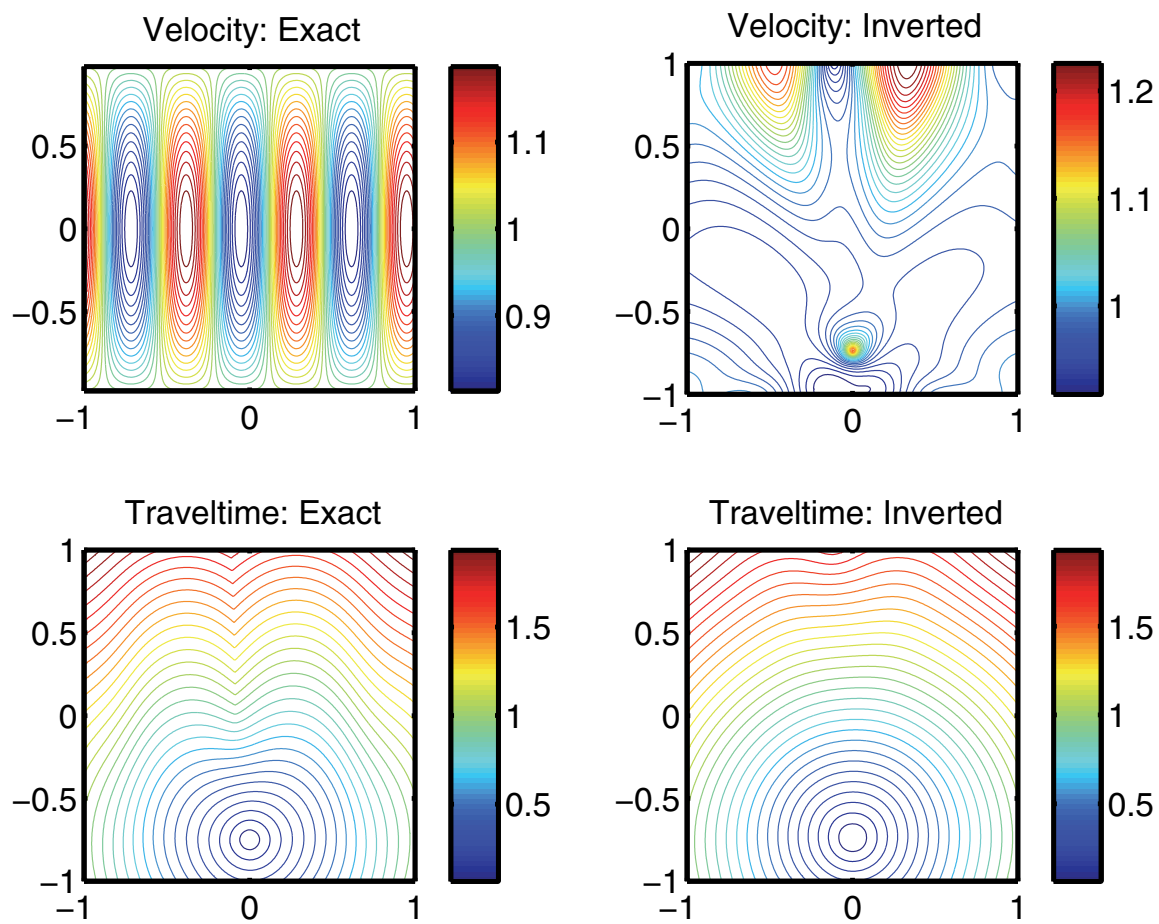
Figure 9. *(Sinusoidal velocity model.) Reconstructed solutions using one point source at $(x_s, y_s) = (0, -0.75)$ on the mesh $\Delta x = \Delta y = 1/128$. Top row: the velocity. Bottom row: the traveltime field.*
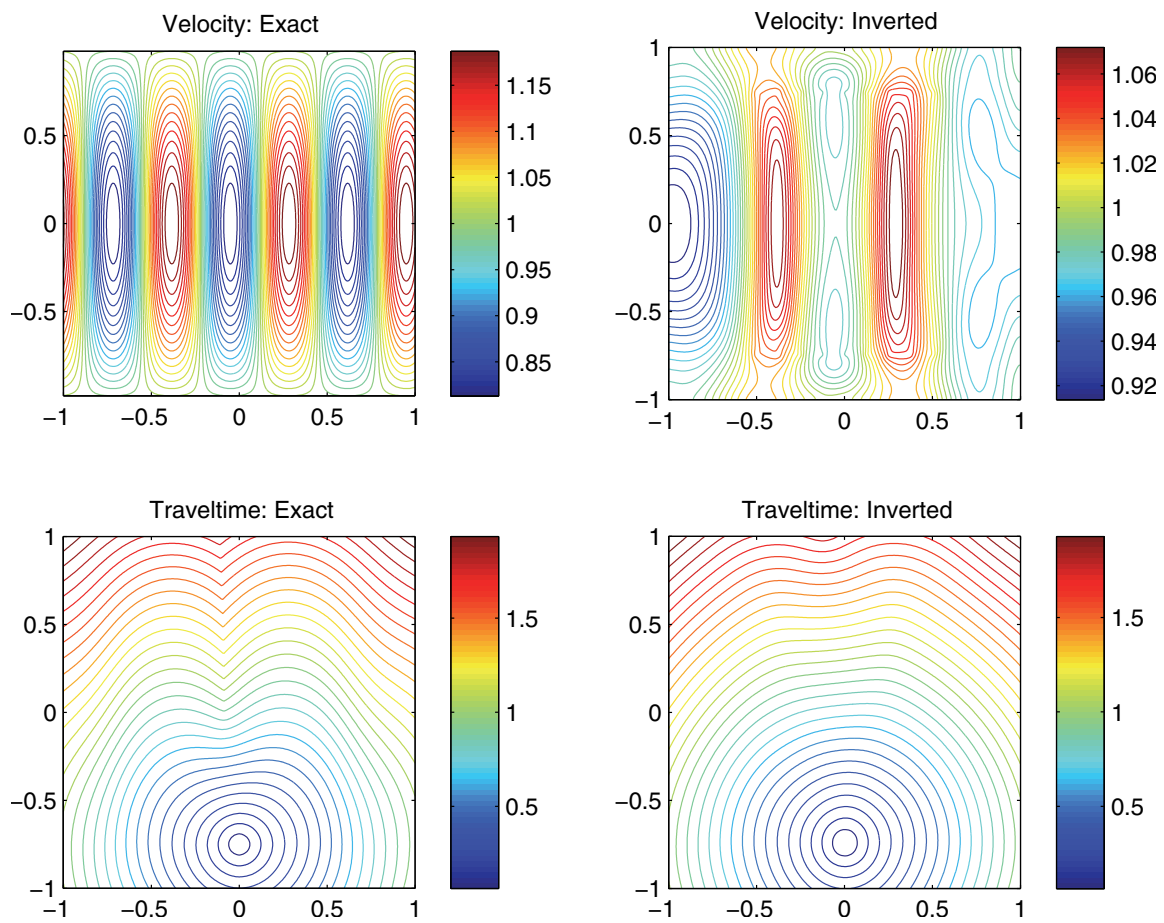
Figure 10. *(Sinusoidal velocity model.) Reconstructed solutions using* 18 *point sources on the mesh* $\Delta x = \Delta y = 1/128$. *The velocity (top row) and the traveltime field (bottom row) corresponding to the source* $(x_s, y_s) = (0, -0.75)$.
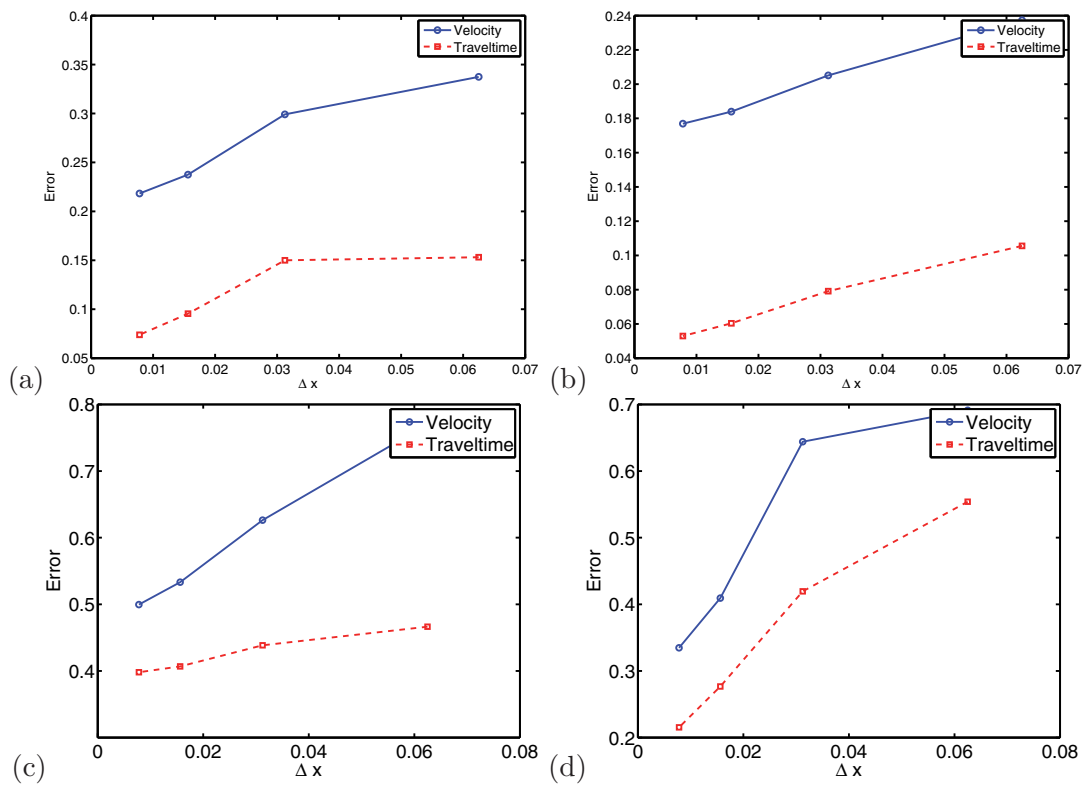
Figure 11. *(Sinusoidal velocity model.) Error in the reconstructed velocity and the approximate traveltime field using* (a) *one and* (b) 18 *point sources with complete measurements. Error in the reconstructed velocity and the approximate traveltime field using* (c) *one and* (d) 18 *point sources with measurements on y = 1 only.*

Table 1
E_{vel} and E_{tra} for the Marmousi model with different number of point sources.

Number of sources	10	20	28
E_{vel}	0.62941	0.62468	0.60780
E_{tra}	1.12971	0.03696	0.03565

6.4. The Marmousi model. This test case is the Marmousi model from the INRIA Workshop on multiarrival traveltimes. The original Marmousi model is sampled on a 0.024km-by-0.024km grid, consisting of 384 samples in the x-direction and 122 samples in the y-direction. In the computational results here, we use only a portion of the data, i.e., a window from 4.584km to 7.488km in the x-direction and from 0km to 2.904km in the y-direction. We have carried out numerical experiments for three different sets of sources. Using the standard MATLAB colon notation, we place the first set of 10 point sources at $(x_s, y_s) = (5.136 : 0.576 : 7.440, y_{1,2})$, where $y_1 = 0.096$ and $y_2 = 2.808$. To increase the resolution in the solution, the second set of sources consists of 20 sources located at $(x_s, y_s) = (4.848 : 0.288 : 7.440, y_{1,2})$. The third set of point sources consists of the second set and eight more point sources specified by $(x_s, y_s) = (4.848, 0.408 : 0.288 : 2.424)$.

As illustrated in [38, 25, 26], this model shows multiple arrivals and caustics for many source-receiver configurations so that the underlying metric is not simple. Therefore, this example serves to illustrate the performance of the new tomography algorithm when recovering nonsimple metrics by using only first-arrivals.

Figure 12 shows the reconstructed solution for the third set of point sources with 28 point sources, and we can see that the new tomography algorithm can only recover the velocity field qualitatively well with the macroscopic scale captured correctly. However, because the underlying velocity model is not simple, the first-arrival based tomography yields limited resolution. In terms of traveltimes, we compare that obtained by the direct eikonal solver with that obtained by the tomography algorithm at the point source $(x_s, y_s) = (6.288, 0.096)$, and the two traveltimes are qualitatively similar.

Moreover, we also compute the L_2-error of the solution using (6.1), and we show these errors in Table 1. By increasing the number of sources from 10 to 20, the mismatching errors in the traveltime field are significantly reduced. However, since we are only using first-arrival traveltimes for the inverse problem, we found that the algorithm can only recover the velocity field qualitatively well with the macroscopic scale captured correctly. When we increase the number of sources to 28, the extra information incorporated into the inverse problem does not significantly improve the resolution in the reconstructed velocity. We remark that the inversion result of the Marmousi velocity model is consistent with that obtained by the adjoint-state method described in [14].

6.5. Energy change. Figure 13 illustrates the changes in the energy during iterations for different models. For all test examples, the algorithm converges in $O(10^3)$ iterations. As we can see from these energy plots, which are in the log-log scale, the changes in the energy can all be fitted by straight lines. This exponential decay in the energy can be explained by the fact that the overall algorithm is developed based on the idea of gradient flow.
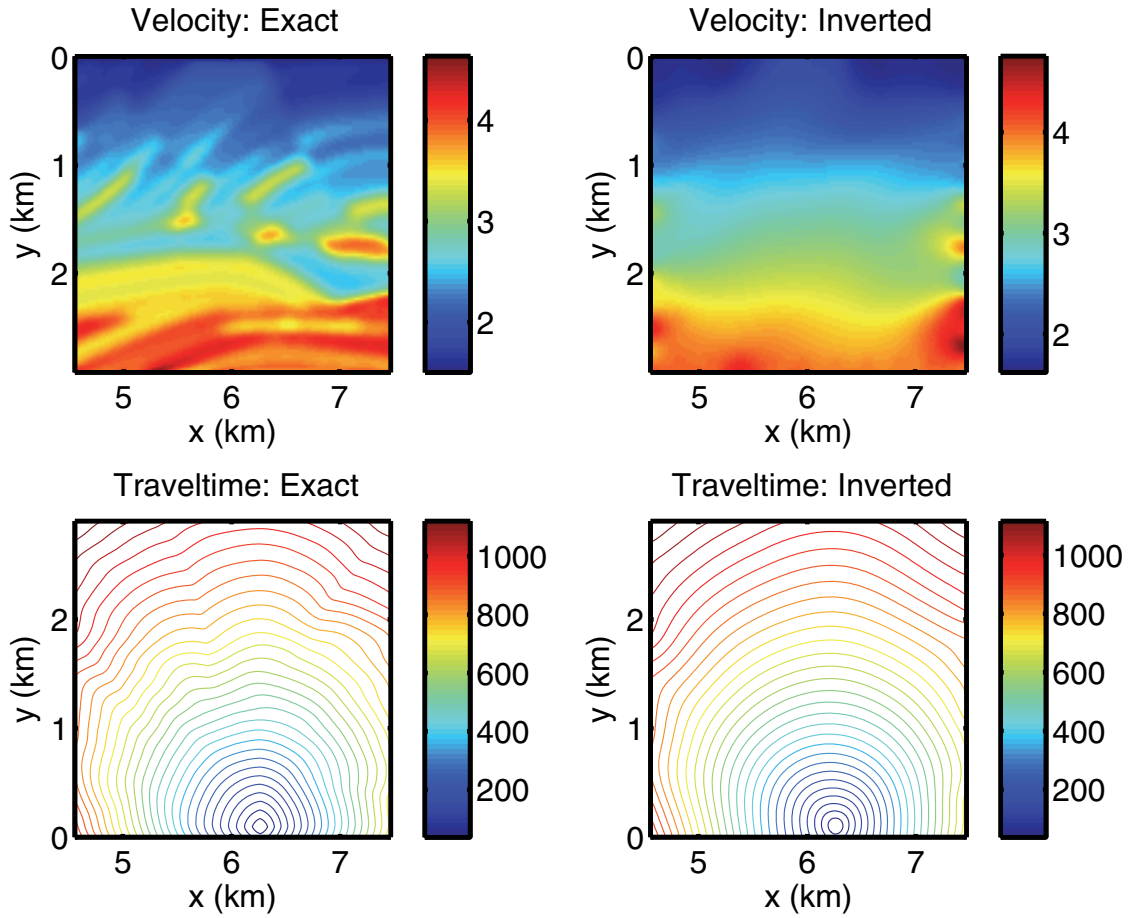
Figure 12. *(Marmousi velocity model with* 28 *point sources.) Reconstructed solutions using* 28 *point sources. The velocity (top row) and the traveltime field (bottom row) corresponding to the source* $(x_s, y_s) = (6.288, 0.096)$.

7. Conclusion. A new methodology is developed for carrying out eikonal based traveltime tomography arising from important applications such as seismic imaging and medical imaging. The new method formulates the traveltime tomography problem as a variational problem of a certain cost functional explicitly with respect to both traveltime and sound speed. Furthermore, the cost functional is penalized to enforce the nonlinear equality constraint associated with the underlying eikonal equation, biharmonically regularized with respect to traveltime, and harmonically regularized with respect to sound speed. To overcome the difficulty associated with the inherent nonlinearity of the eikonal equation, the Euler–Lagrange equation of the penalized-regularized variational problem is reformulated into an equivalent, mixed optimality system. This mixed system is associated with an initial value problem, which is solved by an operator-splitting based solution method, and the splitting approach effectively reduces the optimality system into three nonlinear subproblems and three linear subproblems. Moreover, the nonlinear subproblems can be solved pointwise, and the linear subproblems can be reduced to linear second-order elliptic problems. Numerical experiments show that the new method can carry out traveltime tomography successfully and recover sound speeds efficiently.
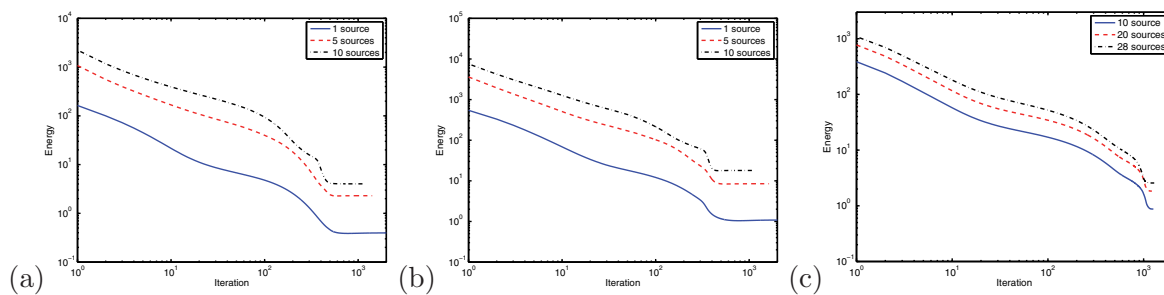
Figure 13. *Change in the energy for* (a) *the linear model,* (b) *the sinusoidal model, and* (c) *the Marmousi model.*

REFERENCES

[1] C. Ammon and J. Vidale, *Tomography without rays*, Bull. Seis. Soc. Am., 83 (1993), pp. 509–528.

[2] E. Chung, J. Qian, G. Uhlmann, and H. Zhao, *A new phase space method for recovering index of refraction from travel times*, Inverse Problems, 23 (2007), pp. 309–329.

[3] E. Chung, J. Qian, G. Uhlmann, and H. Zhao, *An adaptive phase space method with application to reflection traveltime tomography*, Inverse Problems, 27 (2011), 115002.

[4] M. G. Crandall and P. L. Lions, *Viscosity solutions of Hamilton-Jacobi equations*, Trans. Amer. Math. Soc., 277 (1983), pp. 1–42.

[5] B. Dacorogna, R. Glowinski, Y. Kuznetzov, and T. W. Pan, *On a conjugate gradient/Newton/penalty method for the solution of obstacle problems. Application to the solution of an eikonal system with Dirichlet boundary conditions*, in Conjugate Gradient Algorithms and Finite Element Methods, Springer-Verlag, Berlin, Heidelberg, 2004, pp. 263–283.

[6] R. Glowinski, *Finite Element Method for Incompressible Viscous Flow*, Handbook of Numerical Analysis IX, Elsevier, Amsterdam, 2003.

[7] R. Glowinski, *Numerical Methods for Nonlinear Variational Problems*, 2nd ed., Springer-Verlag, New York, 2008.

[8] R. Glowinski, *Variational Methods for the Numerical Solution of Nonlinear Elliptic Problems*, SIAM, Philadelphia, 2015.

[9] R. Glowinski, E. J. Dean, G. Guidoboni, L. H. Juarez, and T.-W. Pan, *Applications of operator-splitting methods to the direct numerical simulation of particulate and free-surface flows and to the numerical solution of the two-dimensional elliptic Monge-Ampere equation*, Japan J. Indust. Appl. Math., 25 (2008), pp. 1–63.

[10] J. Hole and B. C. Zelt, *3-D finite-difference reflection traveltimes*, Geophys. J. Internat., 121 (1995), pp. 427–434.

[11] J.-W. Huang and G. Bellefleur, *Joint transmission and reflection traveltime tomography using the fast sweeping method and the adjoint-state technique*, Geophys. J. Internat., 188 (2012), pp. 570–582.

[12] C. Y. Kao, S. Osher, and J. Qian, *Legendre transform based fast sweeping methods for static Hamilton-Jacobi equations on triangulated meshes*, J. Comput. Phys., 227 (2008), pp. 10209–10225.

[13] C. Y. Kao, S. J. Osher, and J. Qian, *Lax-Friedrichs sweeping schemes for static Hamilton-Jacobi equations*, J. Comput. Phys., 196 (2004), pp. 367–391.

[14] S. Leung and J. Qian, *An adjoint state method for three-dimensional transmission traveltime tomography using first-arrivals*, Comm. Math. Sci., 4 (2006), pp. 249–266.

[15] S. Leung and J. Qian, *Transmission traveltime tomography based on paraxial Liouville equations and level set formulations*, Inverse Problems, 23 (2007), pp. 799–821.

[16] W. Li and S. Leung, *A fast local level set based adjoint state method for first arrival transmission traveltime tomography with discontinuous slowness*, Geophys. J. Internat., 195 (2013), pp. 582–596.

[17] W. Li, S. Leung, and J. Qian, *A level set-adjoint state method for crosswell transmission-reflection traveltime tomography*, Geophys. J. Internat., 199 (2015), pp. 348–367.

[18] S. LUO, J. QIAN, AND R. BURRIDGE, *High-order factorization based high-order hybrid fast sweeping methods for point-source eikonal equations*, SIAM J. Numer. Anal., 52 (2014), pp. 23–44.

[19] S. LUO, J. QIAN, AND H.-K. ZHAO, *Higher-order schemes for 3-D traveltimes and amplitudes*, Geophysics, 77 (2012), pp. T47–T56.

[20] R. MICHEL, *Sur la rigidite imposee par la longueur des geodesiques [On the rigidity imposed by the length of geodesics]*, Invent. Math., 65 (1981), pp. 71–83.

[21] R. G. MUKHOMETOV, *The reconstruction problem of a two-dimensional Riemannian metric, and integral geometry*, Dokl. Akad. Nauk SSSR, 232 (1977), pp. 32–35 (in Russian).

[22] R. G. MUKHOMETOV, *On a problem of reconstructing Riemannian metrics*, Siberian Math. J., 22 (1982), pp. 420–433.

[23] G. NOLET, *A Breviary of Seismic Tomography*, Cambridge University Press, Cambridge, UK, 2009.

[24] L. PESTOV AND G. UHLMANN, *Two dimensional compact simple Riemannian manifolds are boundary distance rigid*, Ann. Math., 161 (2005), pp. 1093–1110.

[25] J. QIAN AND S. LEUNG, *A level set method for paraxial multivalued traveltimes*, J. Comput. Phys., 197 (2004), pp. 711–736.

[26] J. QIAN AND S. LEUNG, *A local level set method for paraxial geometric optics*, SIAM J. Sci. Comput., 28 (2006), pp. 206–223.

[27] J. QIAN AND W. W. SYMES, *Paraxial eikonal solvers for anisotropic quasi-P traveltimes*, J. Comput. Phys., 173 (2001), pp. 1–23.

[28] J. QIAN AND W. W. SYMES, *An adaptive finite difference method for traveltime and amplitude*, Geophysics, 67 (2002), pp. 167–176.

[29] F. QIN, Y. LUO, K. B. OLSEN, W. CAI, AND G. T. SCHUSTER, *Finite difference solution of the eikonal equation along expanding wavefronts*, Geophysics, 57 (1992), pp. 478–487.

[30] W. A. J. SCHNEIDER, K. RANZINGER, A. BALCH, AND C. KRUSE, *A dynamic programming approach to first arrival traveltime computation in media with arbitrarily distributed velocities*, Geophysics, 57 (1992), pp. 39–50.

[31] A. SEI AND W. W. SYMES, *Gradient calculation of the traveltime cost function without ray tracing*, in SEG Technical Program Expanded Abstracts 1994, Society of Exploration Geophysicists, Tulsa, OK, 1994, pp. 1351–1354.

[32] A. SEI AND W. W. SYMES, *Convergent finite-difference traveltime gradient for tomography*, in SEG Technical Program Expanded Abstracts 1995, Society of Exploration Geophysicists, Tulsa, OK, 1995, pp. 1258–1261.

[33] J. A. SETHIAN AND A. M. POPOVICI, *3-D traveltime computation using the fast marching method*, Geophysics, 64 (1999), pp. 516–523.

[34] P. STEFANOV AND G. UHLMANN, *Boundary rigidity and stability for generic simple metrics*, J. Amer. Math. Soc., 18 (2005), pp. 975–1003.

[35] P. STEFANOV AND G. UHLMANN, *Integral geometry of tensor fields on a class of non-simple Riemannian manifolds*, Amer. J. Math., 130 (2008), pp. 239–268.

[36] P. STEFANOV AND G. UHLMANN, *Local lens rigidity with incomplete data for a class of non-simple Riemannian manifolds*, J. Diff. Geom., 82 (2009), pp. 383–409.

[37] G. STRANG, *On the construction and comparison of difference schemes*, SIAM J. Numer. Anal., 5 (1968), pp. 506–517.

[38] W. W. SYMES AND J. QIAN, *A slowness matching Eulerian method for multivalued solutions of eikonal equations*, J. Sci. Comput., 19 (2003), pp. 501–526.

[39] C. TAILLANDIER, M. NOBLE, H. CHAURIS, AND H. CALANDRA, *First-arrival traveltime tomography based on the adjoint-state method*, Geophysics, 74 (2009), pp. WCB1–WCB10.

[40] Y.-H. R. TSAI, L.-T. CHENG, S. J. OSHER, AND H.-K. ZHAO, *Fast sweeping algorithms for a class of Hamilton–Jacobi equations*, SIAM J. Numer. Anal., 41 (2003), pp. 673–694.

[41] J. VAN TRIER AND W. W. SYMES, *Upwind finite-difference calculation of traveltimes*, Geophysics, 56 (1991), pp. 812–821.

[42] J. VIDALE, *Finite-difference calculation of travel times*, Bull. Seis. Soc. Am., 78 (1988), pp. 2062–2076.

[43] H. K. ZHAO, *Fast sweeping method for eikonal equations*, Math. Comp., 74 (2005), pp. 603–627.